FINITE ELEMENT MODELING OF PRESTRESSED COLD-FORMED STEEL BEAMS

Nicolas Hadjipantelis[1], Leroy Gardner[2], and M. Ahmer Wadee[3]

[1]PhD Candidate, Department of Civil and Environmental Engineering, Imperial College London, South Kensington Campus, London SW7 2AZ, UK. (corresponding author). ORCID: https://orcid.org/0000-0001-6368-4962. Email: n.hadjipantelis15@imperial.ac.uk
[2]Professor of Structural Engineering, Department of Civil and Environmental Engineering, Imperial College London, South Kensington Campus, London SW7 2AZ, UK. Email: leroy.gardner@imperial.ac.uk
[2]Professor of Nonlinear Mechanics, Department of Civil and Environmental Engineering, Imperial College London, South Kensington Campus, London SW7 2AZ, UK. Email: a.wadee@imperial.ac.uk

ABSTRACT

The concept and structural benefits of prestressing cold-formed steel beams are explored in the present paper. The prestressing is applied by means of a high-strength steel cable located within the cross-section of the beam, at an eccentric location with respect to the strong geometric axis. The internal forces generated by the prestressing are opposite in sense to those induced under subsequent vertical loading. Hence, the development of detrimental compressive stresses within the top region of the cold-formed steel beam is delayed and thus the load-carrying capacity of the beam is enhanced. Owing to the pre-camber that is induced along the member during the prestressing stage, the overall deflections of the beam are also reduced significantly. In the present paper, following the description of the proposed concept, finite element (FE) modeling is employed to simulate the mechanical behavior of prestressed cold-formed steel beams during the prestressing and vertical loading stages. Following the validation of the FE modeling approach, a set of parametric studies is conducted, where the influence of the key controlling parameters on the structural benefits obtained from the prestressing process is investigated. The parametric results are utilized to determine how the benefits obtained from the addition of the prestressed cable can be maximized, demonstrating the significant enhancements in the performance of the cold-formed steel beam that can be achieved.

INTRODUCTION

Prestressing can enhance the load-carrying capacity and serviceability performance of cold-formed steel beams, enabling a given section to sustain higher loads or span greater distances, potentially opening up new applications within the construction industry (Hadjipantelis et al. 2018a). This concept involves the application of eccentric prestressing by means of a high-strength steel cable that is located within the bottom hollow flange of the cross-section profile of the cold-formed steel beam. The concept of prestressing steel structures was initially proposed by Magnel (1950), while, more recently, prestressed cables have been employed to enhance the performance of hot-rolled steel structures, for instance, bare steel beams (Belletti and Gasperi 2010; Kambal and

Jia 2018), tubular members (Gosaye et al. 2014; Wang et al. 2017), stayed columns (Wadee et al. 2013; Yu and Wadee 2017) and composite beams (Lorenc and Kubica 2006; Lou et al. 2016).

Owing to their high strength-to-weight ratio, cold-formed steel members offer lightweight and low-carbon structural solutions in construction (Hancock 2016; Schafer 2017). However, as a result of their thin-walled geometry, cold-formed steel members are highly susceptible to instability phenomena, such as local, distortional and global buckling together with their interactions, which limit their load-carrying capacity. In the proposed concept, the occurrence of the aforementioned instability phenomena in cold-formed steel beams is delayed by the prestressing, which imposes initial stresses in the beam that are opposite in sign to the stresses induced during the subsequent vertical loading stage. Since these initial stresses need to be overcome first before detrimental compressive stresses develop during loading, the cold-formed steel beam can carry increased loading before failure occurs. The enhanced load-carrying performance of prestressed cold-formed steel beams enables the use of smaller cross-sections for a given demand in capacity, hence material savings are achieved. Furthermore, the overall deflections of the member are reduced significantly due to the pre-camber that is naturally induced by the eccentric prestressing force. The contribution of the cable to the system bending stiffness reduces the overall deflections further. Hence, the prestressed cold-formed steel beams show an enhanced serviceability performance.

Alongside the conceptual development of the prestressed cold-formed steel beams, the authors have developed a set of linear elastic analytical expressions that describe the mechanical behavior of the proposed beams during both the prestressing and the vertical loading stages (Hadjipantelis et al. 2018a). Failure criteria, based on linear interaction equations in conjunction with the Direct Strength Method (DSM), have also developed, whereby the capacities of the cold-formed steel beam and prestressing cable are checked in both loading stages (prestressing and imposed vertical loading). Moreover, finite element (FE) modeling has also been employed to simulate the behavior of the proposed beams, demonstrating an enhancement of 15% in the ultimate moment capacity of the studied reference cold-formed steel beam, as well as a reduction of 60% in the overall deflections (Hadjipantelis et al. 2018a).

The purpose of the present paper is to investigate the influence of the key controlling parameters on the behavior of prestressed cold-formed steel beams, with the aim of maximizing the benefits that can be obtained from the addition of the prestressed cable. Firstly, the mechanical response and failure modes of the proposed beams are discussed briefly. Subsequently, the development and validation of the FE models are presented. A set of parametric studies investigating the effect of the prestress level, cable size, section slenderness and centroid location are presented. Finally, the parametric results are utilized to determine how the obtained benefits can be maximized, demonstrating the significant enhancements in the structural performance of the cold-formed steel beam that can be achieved. Conclusions are then drawn.

CONCEPTUAL DEVELOPMENT AND LOADING STAGES

The conceptual development of prestressed cold-formed steel beams, alongside a detailed analysis of their mechanical behaviour, have been presented in (Hadjipantelis et al. 2018a; Hadjipantelis et al. 2018b); the key features of the proposed concept are briefly discussed below.

Characteristics of Prestressed Cold-formed Steel Beams

The cross-section profile of the proposed beams is shown in Fig. 1(a), where the high-strength steel cable is located within the bottom hollow flange, at an eccentricity e relative to the strong

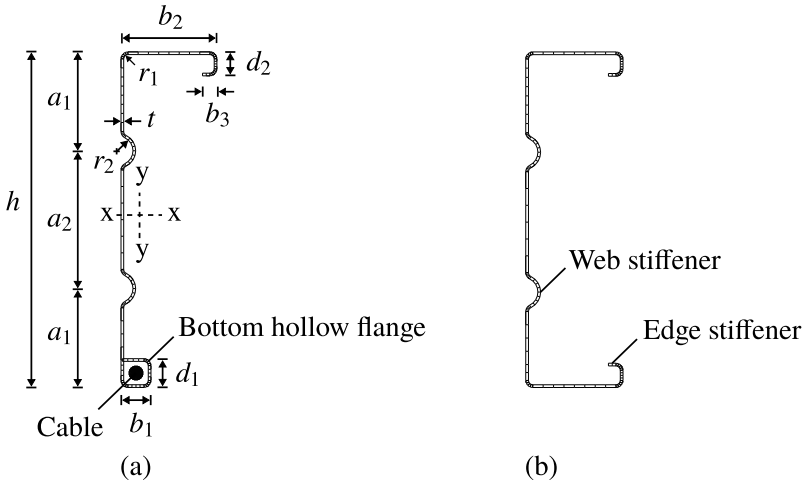


Fig. 1. (a) Cross-section profile of the proposed prestressed cold-formed steel beams. (b) Lipped channel section with web and edge stiffeners tested by Kyvelou et al. (2017).

geometric (x–x) axis of the cross-section. Similar profiles are currently being used in practice, such as that tested by Kyvelou et al. (2017), as shown in Fig. 1(b). The edge of the bottom hollow flange is assumed herein to be tied to the web by means of welding or screws.

The cable is tensioned using a jacking mechanism and anchored at the two beam ends, while, along the member, the cable is kept concentric to the bottom hollow flange either by a snug fit or by means of connecting collars that are attached to the cable at regular intervals along its length. The cable is allowed to elongate freely, thus the axial force within the cable remains constant along its length (Hadjipantelis et al. 2018a). Furthermore, the proposed beams are assumed to be fully braced against lateral-torsional buckling due to the presence of floor sheeting and sag bars at regular intervals along the member that interconnect the top and bottom flanges of the beam with those of the adjacent beams. Note that, these lateral restraints also confine bending about the strong geometric axis of the cross-section, thus preventing any asymmetric bending effects.

Loading Stages

Two loading stages are considered. In Stage I, the initial prestressing force P_i is transmitted into the cold-formed steel beam as an eccentric compression, thus inducing a pre-camber along the member, as illustrated in Fig. 2. In Stage II, vertical loading is imposed in the form of uniformly distributed loading, inducing a maximum bending moment at midspan M_max. As illustrated in Fig. 2, the imposed loading counteracts the pre-camber from Stage I, while, as the beam deforms downwards, the cable is stretched further since it is located below the neutral axis of the section. This results in an incremental increase in the prestressing force ΔP, which induces an additional eccentric compression. Eventually, depending on the section slenderness, the member fails due to either yielding or local/distortional buckling of the cold-formed steel beam or due to yielding of the cable in tension (Hadjipantelis et al. 2018a).

The components of the axial stress distribution at the critical section of the beam during the two loading stages are shown in Fig. 3, where A_s and A_c are the cross-sectional areas of the steel beam and cable respectively, while E_s and E_c are the respective Young's moduli; $S_\mathrm{t}{=}I_\mathrm{s}/y_\mathrm{t}$ and $S_\mathrm{b}{=}I_\mathrm{s}/y_\mathrm{b}$ are the elastic section moduli corresponding to first yield of the top and bottom flanges respectively,

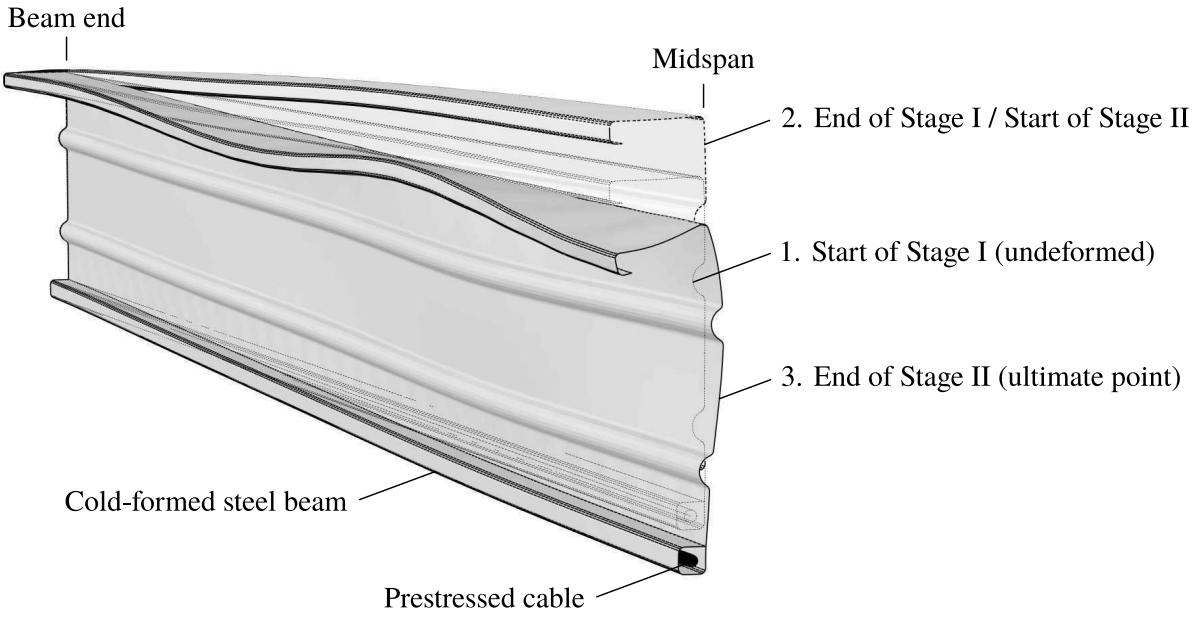


Fig. 2. Section cut at the midspan of the prestressed cold-formed steel beam showing the deformed geometry during the different loading stages. Failure due to distortional buckling.

with I_s being the second moment of area of the bare steel section about its strong geometric axis.

In Stage I, the eccentric compression, which is equivalent to uniform compression plus negative (i.e. hogging) bending, induces a uniform axial compressive and a negative bending stress distribution, as shown in Figs. 3(a) and (b) respectively. At the end of Stage I, tensile (positive) and compressive stresses are induced within the top and bottom flanges of the beam respectively. Note that these initial stresses have an opposite sign to the stresses imposed due to the subsequent vertical loading.

In Stage II, a positive bending stress distribution is imposed at midspan due to M_{max}, as shown in Fig. 3(c), together with axial compressive and negative bending stress distributions due to ΔP, as shown in Figs. 3(d)–(e). The overall stress levels at the top σ_t and bottom σ_b flanges at the end of Stage II can be obtained by superimposing the individual stress components. The benefits from the addition of the prestressed cable originate from the fact that the initial stresses induced in Stage I need to be overcome first during Stage II and, consequently, the development of local/distortional buckling in the compressed region of the beam is delayed. Hence, the beam is able to carry greater loading before detrimental compressive stresses develop, i.e. the load-carrying capacity of the cold-formed steel beam is enhanced.

Failure Modes

Failure of the proposed prestressed system takes place when the load-carrying capacity of either the cold-formed steel beam or the cable is exceeded, in either of the two loading stages. Generally, provided a sufficiently large cable is employed, failure of the prestressed member will be governed by the capacity of the cold-formed steel beam. In Stage I, compressive stresses arise in the bottom flange, as shown in Fig. 4(a), but the geometry of the section is resistant to local/distortional buckling in this region. Meanwhile, the top region of the beam is subjected to tensile stresses. The presence of the prestressed cable and the bottom lateral restraints prevent lateral-torsional and

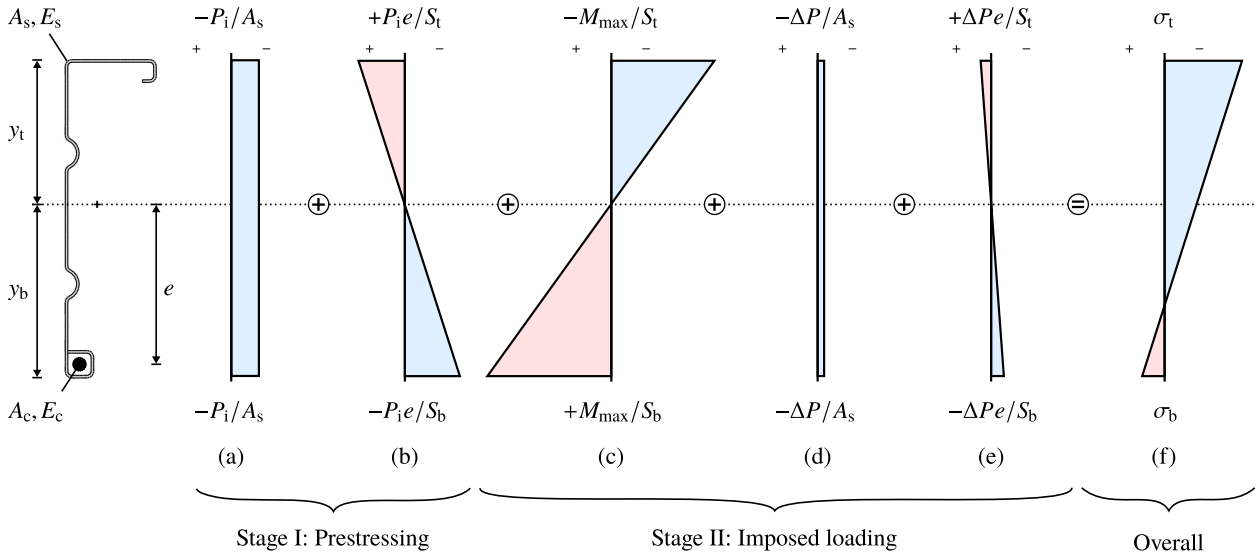


Fig. 3. Components of the midspan axial stress distribution in the two loading stages.

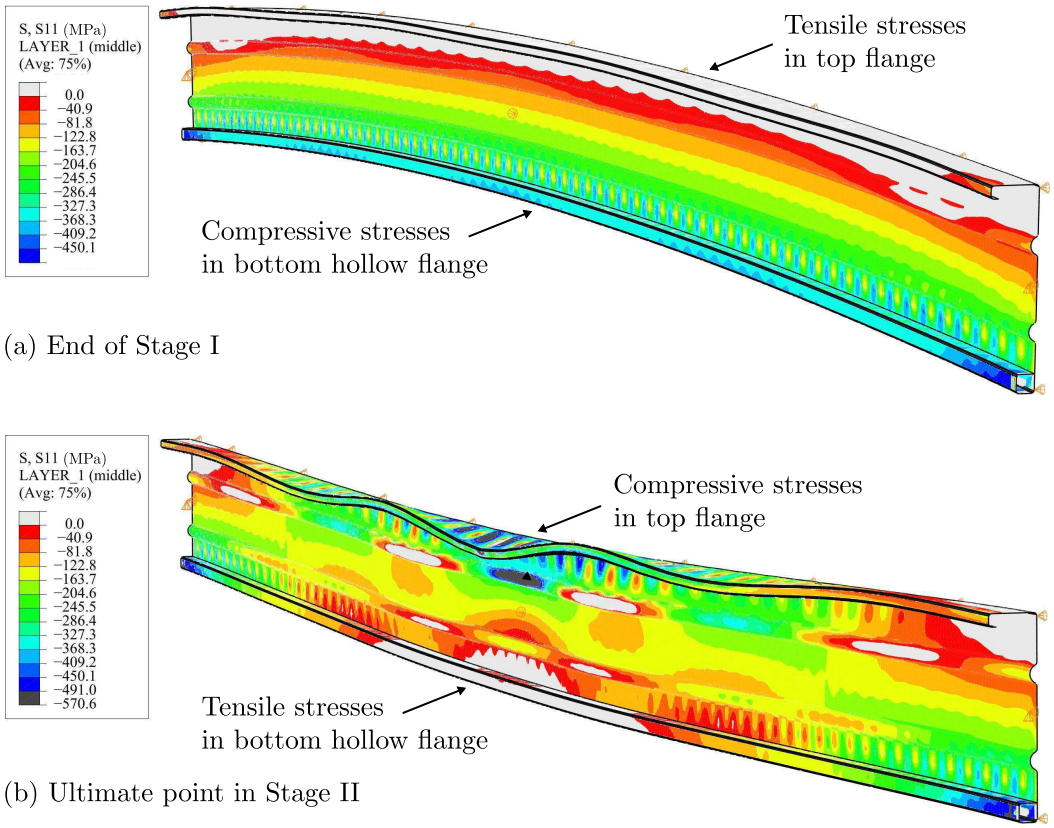


Fig. 4. Illustration of the axial stress levels in prestressed cold-formed steel beams at the end of Stage I and the mode of failure due to the imposed vertical loading in Stage II.

flexural buckling, as discussed above.

In Stage II, the stresses arising from the applied vertical loading counteract the initial stresses induced due to the prestressing, and eventually the top region of the cold-formed steel beam is subjected to compressive stresses, as shown in Fig. 4(b). Failure is then triggered in this region by local buckling, distortional buckling or material yielding, depending on the cross-section proportions. In the case of the studied cross-section profiles, distortional buckling was the predominant mode of failure, as shown in Fig. 4(b).

Design Recommendations

Since the cold-formed steel beam is subjected to a combination of axial force and bending moment during both loading stages, it can be designed as a beam-column using linear interaction equations in conjunction with the Direct Strength Method (DSM) (Schafer 2008; Camotim et al. 2016), as set out in AISI-S100-16 (2016). The cable is designed by checking that the prestressing force does not exceed its tensile capacity. The capacities of both the steel beam and the cable need to be checked during both loading stages by considering the appropriate loading configuration. A more detailed discussion on the design recommendations, including a set of failure criteria, has been presented by the authors of the current paper (Hadjipantelis et al. 2018a), where it was shown that the maximum allowable initial prestressing force P_{max} that the steel beam can carry during Stage I can be predicted using the following equation:

$$P_{\text{max}} = \frac{1}{\left(\dfrac{1}{\phi_{\text{c}} P_{\text{n}}} + \dfrac{e}{\phi_{\text{b}} M_{\text{nx}}^{-}} \right)} , \tag{1}$$

where the axial compressive resistance P_{n} and nominal negative bending resistance M_{nx}^{-} of the steel beam can be determined using the DSM; ϕ_{c} and ϕ_{b} are the resistance factors for compression and bending respectively.

FINITE ELEMENT MODELING

A geometrically and materially nonlinear finite element (FE) analysis with imperfections has been conducted using the commercial package ABAQUS (2014) to simulate the behavior of the prestressed cold-formed steel beams.

Element Types and Meshing Scheme

The steel beam and cable were modeled using S4R shell and T3D2 truss elements (ABAQUS 2014) respectively, with the meshing scheme shown in Fig. 1(a) and a longitudinal mesh size of 10 mm.

Material Modeling

Typically, cold-formed steel follows a rounded nonlinear material response with gradual strain hardening and no distinct yielding point. Hence, the modified two-stage Ramberg–Osgood model has been employed herein to model the constitutive response of the steel beam. Originally developed by Ramberg and Osgood (1943) to capture the nonlinear response of metallic materials, such as aluminium and stainless steel, this model was subsequently modified by several researchers (Hill 1944; Mirambell and Real 2000; Rasmussen 2003), until Gardner and Ashraf (2006) proposed the expressions utilized herein, as given by:

$$\epsilon = \frac{\sigma}{E_s} + 0.002 \left(\frac{\sigma}{\sigma_{0.2}} \right)^{n} \qquad \text{for} \quad \sigma \leqslant \sigma_{0.2} , \tag{2}$$

$$\epsilon = \frac{\sigma - \sigma_{0.2}}{E_{0.2}} + \left(\epsilon_{t1.0} - \epsilon_{t0.2} - \frac{\sigma_{1.0} - \sigma_{0.2}}{E_{0.2}}\right)\left(\frac{\sigma - \sigma_{0.2}}{\sigma_{1.0} - \sigma_{0.2}}\right)^{n'_{0.2,1.0}} + \epsilon_{t0.2} \qquad \text{for} \quad \sigma > \sigma_{0.2}\,, \quad (3)$$

where σ and ϵ are the engineering stress and strain respectively, E_s is the Young's modulus of the cold-formed steel and $E_{0.2}$ is the tangent modulus at the 0.2% proof stress, which is typically taken as the equivalent yield point for design. Moreover, $\epsilon_{t0.2}$ and $\epsilon_{t1.0}$ are the total strains at 0.2% proof stress $\sigma_{0.2}$ and 1.0% proof stress $\sigma_{1.0}$ respectively. The roundedness of the first and second stages of the stress–strain curve is defined by the strain hardening exponents n and $n'_{0.2,1.0}$ respectively. The modified two-stage Ramberg–Osgood model has been utilized in previous research (Haidarali and Nethercot 2011; Hui et al. 2016; Kyvelou et al. 2018; Gardner and Yun 2018) to replicate the nonlinear material response of cold-formed steel members accurately. Recently, Gardner and Yun (2018) analysed an extensive set of material strain data collected from literature to provide predictive expressions for the key input parameters in Eqs. (2) and (3), thus enabling the determination of the full constitutive response of cold-formed steels.

Owing to the development of plastic deformations during the cold-forming process, the corner regions of cold-formed steel members exhibit higher yield and ultimate strengths, as well as lower ductility, than the flat regions (Afshan et al. 2013). In the present study, this effect was included by increasing the 0.2% proof stress of the material within the corner regions $\sigma_{0.2,\text{corner}}$ of the beam, according to $\sigma_{0.2,\text{corner}}$=1.17 $\sigma_{0.2,\text{flat}}$, as determined experimentally by Kyvelou et al. (2018); $\sigma_{0.2,\text{flat}}$ being the 0.2% proof stress within the flat regions. It is worth noting that, following the same approach as Kyvelou et al. (2018), residual stresses through the thickness of the cold-formed steel section were not introduced into the FE models of the present study since their effect is assumed to be inherently included in the constitutive response obtained from the tensile coupon tests (Jandera et al. 2008).

The following material parameters, determined experimentally by Kyvelou et al. (2018) for cold-formed steel beams similar to those studied herein (see Fig. 1(b)), were adopted in the developed FE models: E_s=201 kN/mm^2, $\sigma_{0.2,\text{flat}}$=491 N/mm^2, n=11.2, $n'_{0.2,1.0}$=2.1. The resulting stress–strain response of the cold-formed steel is shown in Fig. 5, together with the elastic, perfectly–plastic material model with no strain hardening that has been employed by the authors to enable direct comparisons to be made between the FE and analytical models (Hadjipantelis et al. 2018a).

The high-strength steel cable was modeled as elastic, perfectly–plastic, as shown in Fig. 5. The plastic part of the material curve was included to enable the identification of cable failure; the FE simulation terminated when the yield stress of the cable was reached. The yield stress of the cable was taken as $F_{y,c}$=1860 N/mm^2 following Gosaye et al. (2014), while the Young's modulus was taken to be E_c=195 kN/mm^2 based on Clause 3.3.6(3) in EN-1992-1-1 (2004) and the research by Madrazo-Aguirre et al. (2015).

Note that, for both materials, the engineering stress and strain values were converted into true stress and logarithmic plastic strain respectively for input into ABAQUS (2014).

Initial Geometric Imperfections

The behavior of cold-formed steel members is sensitive to geometric imperfections, hence perturbations were imposed on the initially perfect geometry of the cold-formed steel members. The shape and distribution of the imperfections were based on the critical local and distortional buckling modes of the beam, which were obtained using the finite strip software CUFSM (Li and Schafer 2010). Note that the lateral-torsional and negative bending distortional buckling modes are restrained in the proposed beams by lateral bracing and the cable; hence, the imperfections

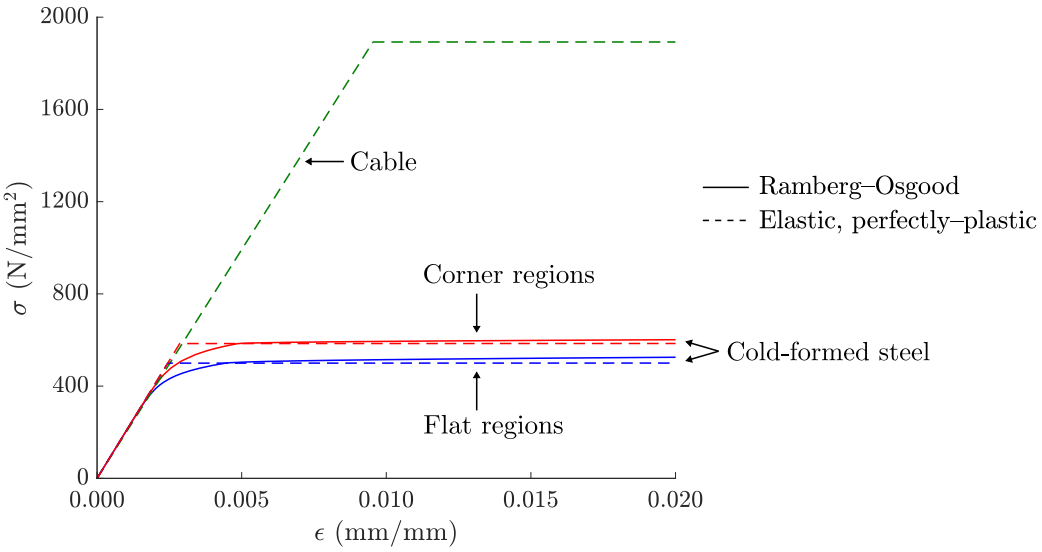


Fig. 5. Initial part of the material stress–strain curves for the flat and corner regions of the cold-formed steel beam and the equivalent for the high-strength steel cable.

corresponding to these modes were not introduced. To account for the loading configurations of Stages I and II (i.e. compression plus negative and positive bending respectively), the imperfection shapes were obtained by applying negative and positive bending stress distributions in CUFSM respectively. The deformed shapes, shown in Fig. 6, were then extracted and scaled according to their respective maximum imperfection magnitudes, which were based on the cumulative distribution functions (CDFs) proposed by Schafer and Peköz (1998). As often adopted in the literature (Yu and Schafer 2007; Haidarali and Nethercot 2011; Shifferaw and Schafer 2012), the magnitudes consistent with a CDF value of 50% have been employed herein, as shown in Fig. 6. The suitability of this assumption is confirmed in the following section. Subsequently, the imperfections were distributed along the length of beam using sinusoidal functions with the corresponding critical half-wavelengths, and, finally, the three imperfections were superposed.

Boundary and Loading Conditions

The simply-supported boundary conditions at the two member ends were modeled using kinematic coupling (ABAQUS 2014), as shown in Fig. 7(a). For this purpose, the degrees of freedom (DOFs) of the end sections of the beam were linked to reference points, in which the vertical (DOF–2) and out-of-plane (DOF–3) translations were then restrained. Longitudinal rigid body motion of the beam was restrained by means of a DOF–1 boundary condition at a single node at midspan. The bracing against lateral-torsional buckling was modeled by restraining the out-of-plane (DOF–3) translations of the top and bottom nodes of the web, as shown in Fig. 7(a), at regular intervals along the beam.

The prestressing force was induced by means of thermal loading (Hadjipantelis et al. 2018a). It is worth noting that, to account for the initial elastic shortening of the beam and the cable, the prestressing stage was iterated until the desired initial prestress level was achieved. The vertical loading was applied by means of concentrated loads at the junctions between the web and the top flange along the beam, as shown in Fig. 7(a).

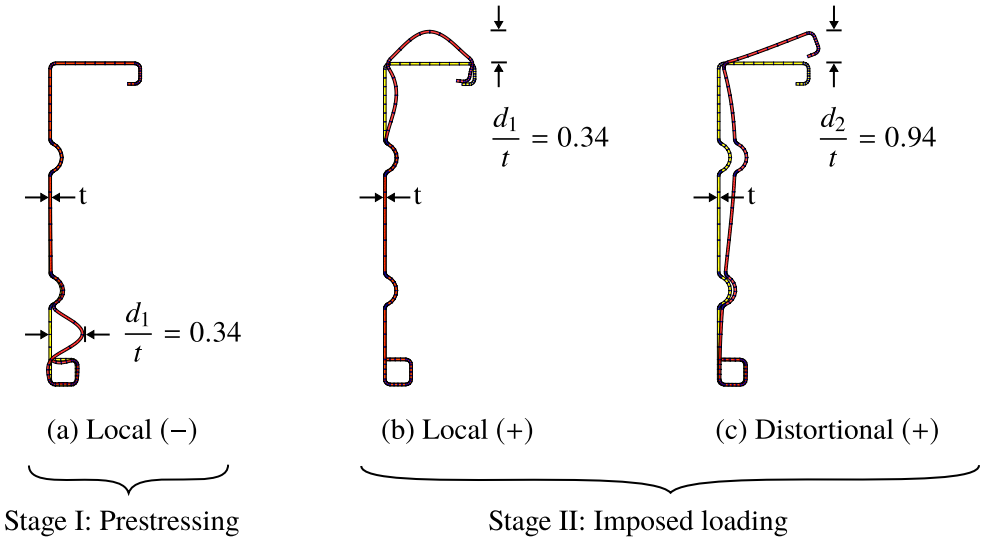


Fig. 6. Characteristics of the initial geometric imperfections corresponding to (a) critical local buckling for negative bending and to critical (b) local and (c) distortional buckling for positive bending.

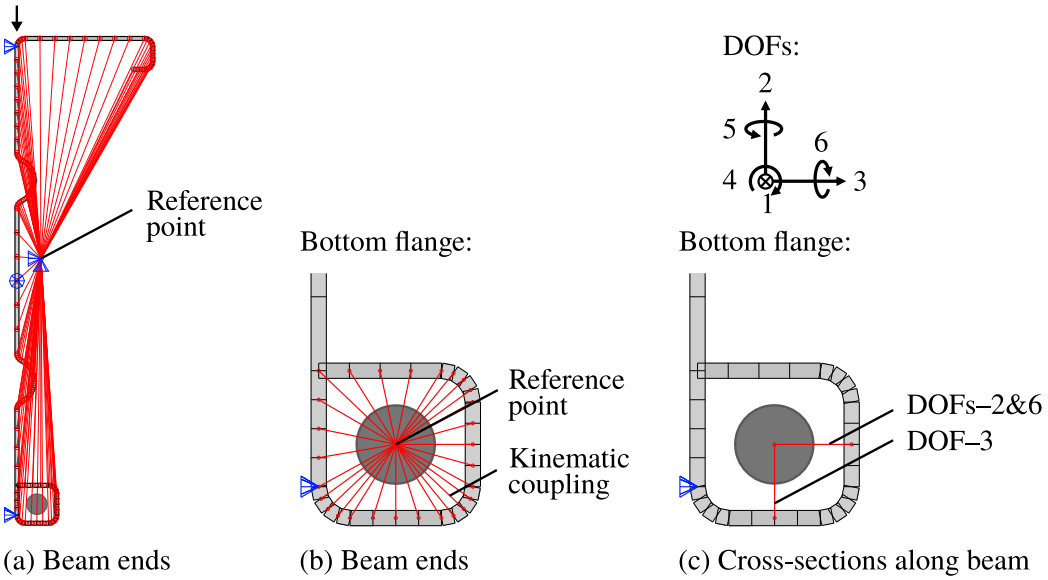


Fig. 7. Modeling of the (a) simply-supported boundary conditions, (b) anchorages at the two beam ends and (c) connection/bond between the steel beam and the cable along the member.

Connection Between Steel Beam and Cable

Kinematic coupling was also employed to model the anchorages at the two beam ends. The end nodes of the bottom hollow flange and the ends of the cable were linked to a reference point, as illustrated in Fig. 7(b), ensuring the uniform transfer of the prestressing force into the entire bottom flange. Constraint equations (ABAQUS 2014) were introduced at every cross-section along the member, linking DOFs–2 and 6 alongside DOF–3 of the cable with the middle side node and middle bottom node of the hollow flange respectively, as shown in Fig. 7(c). In this manner, DOF–1 of the cable remained unconstrained and thus the cable was allowed to elongate freely along the member while being kept concentric to the bottom flange.

Solution Scheme

The prestressing stage was modeled using a geometrically nonlinear 'Static' analysis (ABAQUS 2014), while the imposed loading stage was performed using a 'Static, Riks' analysis (Riks 1979), which is typically employed to model complex geometrically nonlinear responses (Schafer et al. 2010).

VALIDATION OF THE DEVELOPED FINITE ELEMENT MODELS

Since experimental investigations were not within the scope of the present paper, to ensure that the behavior of the prestressed cold-formed steel beams was simulated accurately by the FE models, a combination of validation techniques is employed herein. The adopted validation approach regarding the two structural components of the prestressed system, i.e. the prestressed cable and the cold-formed steel beam, is described below.

Modeling of Prestressed Cable

The modeling approach for the prestressed cable was validated against analytical results, as reported by Hadjipantelis et al. (2018a). Specifically, validation was presented both at member level, in terms of vertical deflections, and at cross-section level, in terms of the axial stress distributions within the cold-formed steel beam and cable. This was performed for three different models, namely bare steel beams, non-prestressed beams (i.e. bare steel beams with a cable but no prestress) and prestressed beams. Furthermore, the FE modeling techniques employed to model the anchorages, the prestressing force and the connection/bond between the steel member and the cable have been successfully utilized by Gosaye et al. (2016) and Wang et al. (2017) to simulate prestressing in prestressed steel tubular members. The numerical models in the aforementioned studies were themselves successfully validated against experimental results.

Modeling of Cold-formed Steel Beam

The performance of cold-formed steel beams with the same cross-section profile as that of the proposed beams (see Fig. 1(a)) has not been studied experimentally in the past. Hence, the FE modeling approach adopted to model the cold-formed steel beam is validated herein against experiments on cross-sections that are as similar as possible to those of the proposed beams. Specifically, the experimental investigations of Yu and Schafer (2006) and Wang and Zhang (2009), in which lipped channel cross-sections were tested in bending, have been chosen. Although the tested cross-sections are not identical to those modeled herein, the sizes, proportions, material properties and failure modes (i.e. local and distortional buckling) are similar. Further validation of the general approach to the modeling of the cold-formed steel cross-sections adopted herein is presented in Kyvelou et al. (2017). The experimental loading arrangement adopted by Yu and

Schafer (2006) and Wang and Zhang (2009) was four-point bending; this arrangement is commonly employed in physical laboratory testing due to the convenience of the experimental setup (i.e. two loading jacks or one loading jack and a spreader beam) and broadly reflects the parabolic bending moment distribution arising under uniform gravity loading, as modeled herein.

Comparisons against the results of the aforementioned experimental studies are presented in the following two sub-sections.

Yu and Schafer (2006) distortional buckling tests

Following a series of local buckling tests (Yu and Schafer 2003), Yu and Schafer conducted 15 further tests to investigate the distortional failure of cold-formed steel lipped channel beams in bending (Yu and Schafer 2006). In this study, the beams were simply-supported and tested in pairs under four-point bending. The bottom flanges of the beams were interconnected along the entire span, while the top flanges were braced only along the shear (i.e. the first and third) spans. For the purposes of validation, only one of the cold-formed steel beams from each tested pair was modeled since the set up was symmetrical. The features of the FE models simulating the Yu and Schafer (2006) tests are illustrated in Fig. 8. The material response of each specimen was extracted from

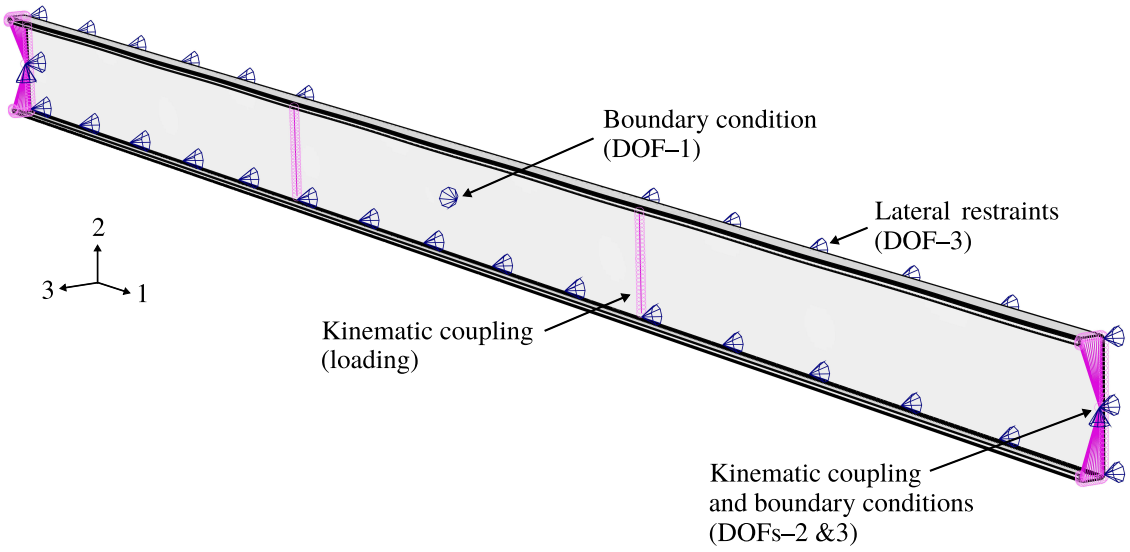


Fig. 8. FE model simulating the four-point bending tests by Yu and Schafer (2006).

the reported stress–strain curves (Yu and Schafer 2005) while the initial geometric imperfections were modeled using the approach described in the previous section. With the aim of conducting an imperfection sensitivity study, three different imperfection magnitudes corresponding to the CDF values of 25%, 50% and 75% were used, as listed in Table 1.

The validation results for the Yu and Schafer (2006) experiments are summarized in Table 2, where the ultimate moment achieved in the FE models M_{FE} is compared with the test results M_{test} and the DSM predictions M_{DSM}. Note that the listed values of the local $\lambda_{\text{l}}=\sqrt{M_{\text{y}}/M_{\text{crl}}}$ and distortional $\lambda_{\text{d}}=\sqrt{M_{\text{y}}/M_{\text{crd}}}$ section slendernesses were based on the reported elastic critical local M_{crl} and distortional M_{crd} buckling moments, as determined by Yu and Schafer (2006) using CUFSM; M_{y} is the yield moment. Overall, excellent agreement is observed between the FE and test results, with a mean $M_{\text{FE}}/M_{\text{test}}$ value of 0.99. The FE models also show excellent agreement with

TABLE 1. Imperfection magnitudes corresponding to the modeled imperfection magnitudes; d_1 and d_2 are defined in Fig. 6.

	25% CDF	50% CDF	75% CDF
d_1/t	0.14	0.34	0.66
d_2/t	0.64	0.94	1.55

TABLE 2. Summary of the validation results for the Yu and Schafer (2006) experiments. Comparisons of the FE results with the test results and DSM predictions.

Model no.	Test label	λ_l or λ_d	M_{FE}/M_{test}	M_{FE}/M_{DSM}	M_{test}/M_{DSM}	Failure mode
1	D8C097-7E6W	0.93	1.00	0.99	0.99	Distortional buckling
2	D8C097-5E4W	–	–	–	–	Lateral-torsional buckling
3	D8C085-2E1W	0.79	0.91	0.99	1.09	Distortional buckling
4	D8C068-6E7W	1.08	1.02	0.91	0.89	Distortional buckling
5	D8C054-7E6W	0.97	1.00	1.00	1.00	Distortional buckling
6	D8C045-1E2W	1.14	1.08	1.05	0.97	Local buckling
7	D8C043-4E2W	1.12	1.05	1.04	0.99	Distortional buckling
8	D8C033-1E2W	1.16	1.07	1.12	1.05	Local buckling
9	D12C068-10E11W *	1.09	0.83	0.98	1.18	Distortional buckling
10	D12C068-1E2W **	–	–	–	–	
11	D10C068-4E3W	0.78	0.93	0.94	1.01	Distortional buckling
12	D10C056-3E4W **	–	–	–	–	
13	D10C048-1E2W	1.26	1.08	1.10	1.02	Distortional buckling
14	D6C063-2E1W	0.91	1.00	1.02	1.02	Distortional buckling
15	D3.62C054-3E4W	0.72	0.84	0.90	1.07	Material yielding
		Mean	0.99	1.00	1.02	
		c.o.v.	0.09	0.07	0.07	

* Unexpected sharp drop in test result during loading.

** Beam damaged prior to testing, hence the test was not modeled.

the DSM predictions, with a mean M_{FE}/M_{DSM} value of 1.00 being achieved. The low coefficient of variation (c.o.v.) values indicate that there is a low degree of scatter in the results. Note that test 2 was not included in the comparisons since, during testing, the beam failed due to lateral-torsional buckling (Yu and Schafer 2006). Similarly, tests 10 and 12 were not modeled since, according to (Yu and Schafer 2005) and (Yu and Schafer 2006) respectively, the beams were damaged prior to testing.

Wang and Zhang (2009) four-point and three-point bending tests

An experimental and numerical investigation into the behavior of 12 cold-formed steel beams subjected to four-point and three-point bending was conducted by Wang and Zhang (2009). The beams had a channel or lipped channel cross-section with different types of edges and were tested in pairs. In the four-point bending tests, the two beams were not interconnected within the constant

moment region, while, in the three-point bending tests, bracing was introduced only along one half of the beam length.

Eight of the beam tests were modeled herein, four in four-point bending and four in three-point bending. As recommended by Wang and Zhang (2009), a bilinear stress–strain curve was employed, with the reported average yield stress and Young's modulus values being used. Furthermore, the reported average values of the imperfection magnitudes were utilized. The results are summarized in Table 3, where excellent agreement between the FE and test results may be seen.

TABLE 3. Summary of the validation results for the Wang and Zhang (2009) experiments. Comparisons of the FE with the corresponding test results.

Model no.	Test label	Cross-section profile	Loading configuration	λ_d	M_{FE}/M_{test}
1	L_CH200B8Od30a20	Lipped C with edge stiffeners	4-point bending	0.60	0.95
2	L_CH200B8Od35a15	Lipped C with edge stiffeners	4-point bending	0.60	0.94
3	L_UH200B80d20	Lipped C	4-point bending	0.74	0.91
4	L_UH200B80d40	Lipped C	4-point bending	0.61	0.95
5	S_CH200B8Od30a20	Lipped C with edge stiffeners	3-point bending	0.55	1.01
6	S_CH200B8Od35a15	Lipped C with edge stiffeners	3-point bending	0.60	1.00
7	S_UH200B80d20	Lipped C	3-point bending	0.75	0.98
8	S_UH200B80d40	Lipped C	3-point bending	0.61	0.99
				Mean	0.97
				c.o.v.	0.04

Overall validation results

The validation FE results are compared with the test results from the investigations of both Yu and Schafer (2006) and Wang and Zhang (2009) in Fig. 9. Overall, good agreement is demonstrated with a mean M_{FE}/M_{test} value of 0.98 and a c.o.v. value of 0.07 being achieved. Note that the results with M_{FE}/M_{test} values of 0.83 and 0.84 correspond to tests where, as indicated in Table 2, an unexpected sharp drop in the readings was observed during the testing (Yu and Schafer 2005), and where, owing to their low slenderness, the beams failed by material yielding (Yu and Schafer 2006) respectively.

The imperfection sensitivity study is represented by the error bars in Fig. 9. The results are summarized in Table 4, where it can be concluded that the FE models with imperfection magnitudes corresponding to a CDF value of 50% provide the most accurate results with respect to the experiments. Hence, the suitability of using this imperfection magnitude for the proposed prestressed beams, as described in the previous section, is confirmed. Note that the imperfection sensitivity was only assessed in the case of the Yu and Schafer tests since, in the tests by Wang and Zhang, the measured imperfection magnitudes were utilized.

The validation results are compared with the DSM capacity predictions in Fig. 10, where the strength expressions for local and distortional buckling are represented by the dashed and solid lines respectively. The comparison illustrates good agreement between the FE results and the design provisions. Note that, since the inelastic reserve strength of the beams is not considered,

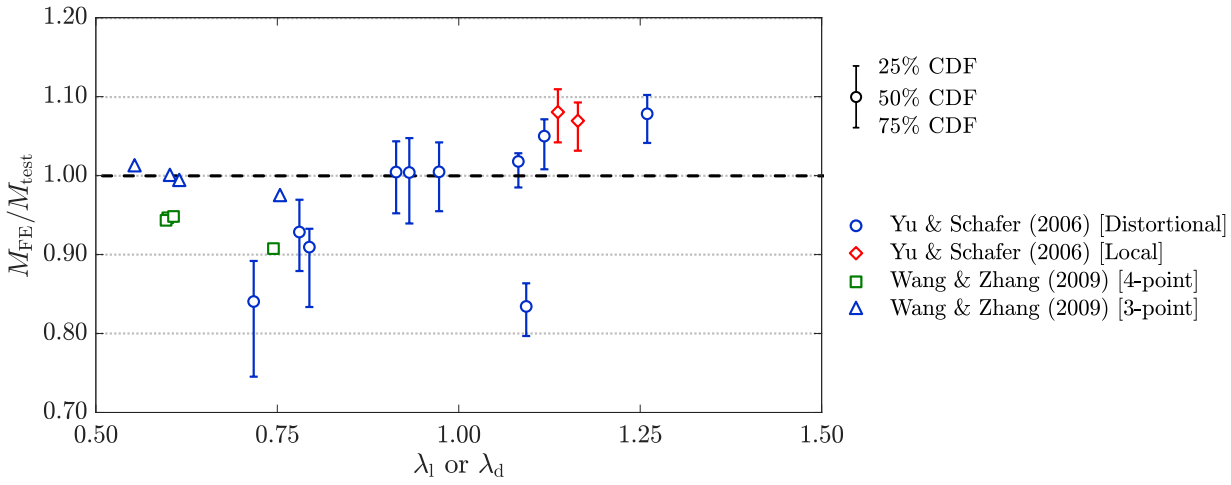


Fig. 9. Comparison between the FE and test results for the validation purposes. Imperfection sensitivity study for the Yu and Schafer (2006) experiments.

TABLE 4. Summary of the results from the imperfection sensitivity study on the tests by Yu and Schafer (2006). The magnitudes corresponding to the CDF values are given in Table 1.

	25% CDF	50% CDF	75% CDF
$(M_{FE}/M_{test})_{mean}$	1.02	0.99	0.93
c.o.v.	0.08	0.09	0.11

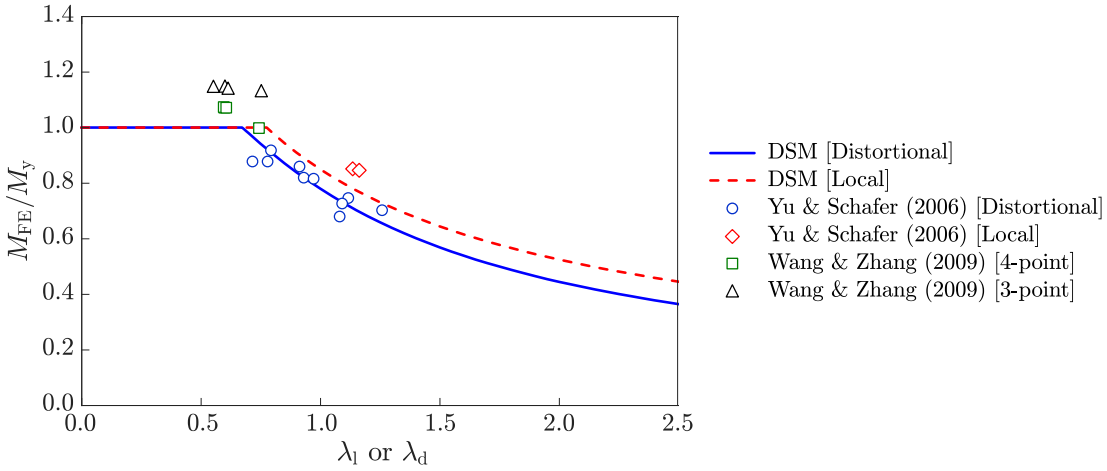


Fig. 10. Comparison between the validation FE results and the local and distortional buckling DSM curves for a beam fully braced against lateral-torsional buckling.

the DSM predictions for the six beams of the Wang and Zhang study with $\lambda_d \leqslant 0.673$ are slightly conservative.

Overall, the excellent agreement between the FE and test results validate the ability of the developed FE models to simulate the cold-formed steel beam component of the proposed system. Based on the validated FE modeling approach, a series of parametric studies is presented in the following section.

PARAMETRIC STUDIES

The purpose of the parametric studies is to investigate the influence of the key controlling parameters on the behavior of the prestressed cold-formed steel beams. Ultimately, the results indicate how these parameters may be optimized and thus how the benefits obtained from the addition of the prestressed cable may be maximized.

Key Controlling Parameters

The parametric studies explore the effect of the prestress level, cable size, section slenderness and centroid location on the benefits obtained from the prestressing, with the respective controlling parameters being P_i/P_{max}, A_c/A_s, t and y_b/h. In each study, the controlling parameter, indicated with an asterisk in Table 5, was varied while the remaining parameters were kept constant. In some cases, in order to keep a parameter constant, its numerator had to be adjusted due to the fact that its denominator is a function of the controlling (variable) parameter; these cases are indicated with the symbol "†" in Table 5.

An example of the notation adopted herein is shown in Fig. 11. The example corresponds to the parametric study regarding the effect of the centroid location, whereby, the cross-section profile of the steel beam was varied while maintaining constant values for both the beam thickness and the cable size. However, since the value of P_{max} depends on the cross-section profile, the initial prestressing force P_i was adjusted accordingly with the aim of keeping the relative prestress level P_i/P_{max} constant.

In the present paper, six cross-section profiles are utilized to study the effect of shifting the centroid location within steel cross-section upwards. The dimensions of the chosen profiles are

TABLE 5. Summary of the variation of the controlling parameters in the parametric studies.

		Prestressing force: P_i/P_{max}	Area: A_c/A_s	Thickness: t	Profile: y_b/h
(i)	Effect of prestress level	$*$	–	–	–
(ii)	Effect of cable size	–	$*$	–	–
(iii)	Effect of section slenderness	†	†	$*$	–
(iv)	Effect of centroid location	†	–	–	$*$

$*$ Controlling (variable) parameter.

– Constant parameter.

† Constant parameter; the denominator is a function of the controlling (variable) parameter and thus the numerator had to be adjusted accordingly to ensure the current parameter is constant.

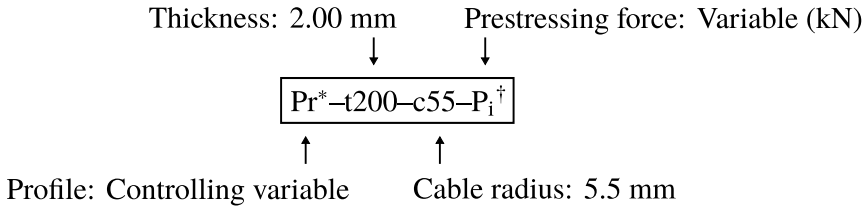


Fig. 11. Example of the notation adopted herein.

TABLE 6. Dimensions of the top and bottom flanges of the chosen profiles, according to Fig. 1(a).

Profile	b_1 (mm)	d_1 (mm)	b_2 (mm)	y_b/h
1	32.0	31.0	60.0	0.50
2	30.0	29.0	65.0	0.51
3	28.0	28.0	70.0	0.52
4	27.0	26.0	75.0	0.53
5	25.0	24.0	80.0	0.54
6	23.0	23.0	85.0	0.55

Note: For all the profiles h=280.0 mm, b_3=12.0 mm, d_2=20.0 mm, a_1=82.5 mm, a_2=115.0 mm, r_1=3.5 mm, r_2=12.0 mm.

listed in Table 6. The centroid location y_b/h was varied by changing the dimensions of the top and bottom flanges, while maintaining the total area and the height of the section to be constant. The resulting profiles are illustrated in Fig. 12. It is worth noting that, as discussed earlier, the presence of top and bottom lateral restraints confines the applied bending about the strong geometric axis. In the studied profiles, the maximum difference between the bending moments about the major principal and strong geometric axes of the cross-section is less than 2% and occurs in the case of Profile 6.

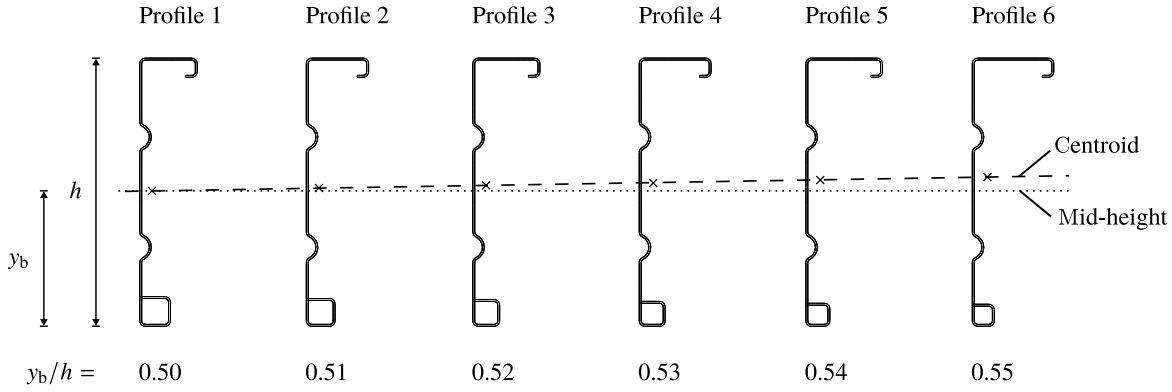


Fig. 12. Cross-section profiles of the cold-formed steel beams used in the parametric studies.

In the following sub-sections, the increase in the ultimate moment capacity of the cold-formed steel beams due to the addition of the prestressed cables is given by the ratio $M_{ult,p}/M_{ult}$, where $M_{ult,p}$

is the ultimate moment at the midspan of the prestressed beam and M_{ult} is the ultimate moment of the bare steel beam. The key properties of the studied beams are listed in Appendix I, alongside the corresponding FE results. Note that distortional buckling is the controlling buckling mode for all the cold-formed steel beam geometries considered in the present work; hence the section slendernesses are given in terms of λ_d herein. Finally, the length of the member in all models was 4800 mm.

Effect of Prestress Level

The prestress level was controlled using the normalized parameter P_i/P_{max}, where, for a given beam geometry, P_i, i.e. the initial prestressing force, was variable and P_{max}, i.e. the maximum allowable prestressing force, as defined in Eq. 1, was constant. As shown in Table 5, the geometry of the cold-formed steel beam and the size of the cable were maintained to be constant; the contribution of the cable to the system is given by A_c/A_s=10.5%. The results presented below correspond to the models Pr4–t200–c55–P_i^*, where the P_{max} was equal to 109 kN. The initial prestressing force was varied to give the following prestress levels:

$$P_i/P_{max} = \{0.0, 0.2, 0.4, 0.6, 0.8, 0.9, 1.0, 1.1, 1.2, 1.3, 1.4\} \ . \tag{4}$$

As discussed in the design recommendations section, the value of P_{max} was determined using the predicted load-carrying capacity of the cold-formed steel beam when subjected to the loading configuration of Stage I. To investigate whether higher prestress levels than P_{max} could actually be carried, and whether these levels offered greater benefits, prestress levels up to 1.4 times P_{max} were modeled herein; these results are shown with dashed lines in the figures below.

The normalized moment–deflection responses of the Pr4–t200–c55–P_i^* models are shown in Fig. 13(a), where M_y is the yield moment of the bare steel beam, δ_{mid} is the vertical deflection at the member midspan and $\delta_{mid,y}$ is the midspan vertical deflection at the first yield point. Note that only the results corresponding to P_i/P_{max}=$\{0.0, 0.2, 0.4, 0.6, 0.8, 1.0, 1.2, 1.4\}$ and the bare steel beam are shown. Firstly, it is observed that as the prestress level is increased, the pre-camber (i.e. the starting point of the response) induced during Stage I also increases, and thus the overall vertical deflections of the member at failure decrease. Secondly, as the level of prestress is increased, the ultimate moment capacity of the beam is enhanced further.

To explain the increase in capacity, Figs. 13(c) and (d) can be utilized, whereby the normalized moment–stress responses corresponding to the top and bottom flanges respectively are shown; $\sigma_{t,av}$ and $\sigma_{b,av}$ are the average membrane stress levels within the top and bottom flanges respectively, while $F_{y,s}$ is the yield stress of the cold-formed steel. Note that failure of the steel beam can be predicted using the DSM failure stress $\sigma_{t,DSM}$ (Hadjipantelis et al. 2018a), which is indicated by the vertical dotted line in Fig. 13(c) and is defined as $\sigma_{t,DSM} = M_{nx}^+/S_t$, where M_{nx}^+ is the DSM moment capacity prediction for the bare steel beam when subjected to pure positive bending. As shown in Fig. 13(c), the higher the prestress level, the greater the tensile stresses within the top flange at the start of Stage II. Since these initial tensile stresses have to be first overcome before compressive stresses can develop and $\sigma_{t,DSM}$ is reached, a greater moment is required to cause the failure of the cold-formed steel beam. Hence, the higher the prestress level, the more the occurrence of local/distortional buckling is delayed and thus the greater the moment capacity enhancement. Furthermore, as shown in Fig. 13(d), owing to the high compressive stress levels induced within the bottom flange during the prestressing, the utilization of the bottom flange decreases with increasing

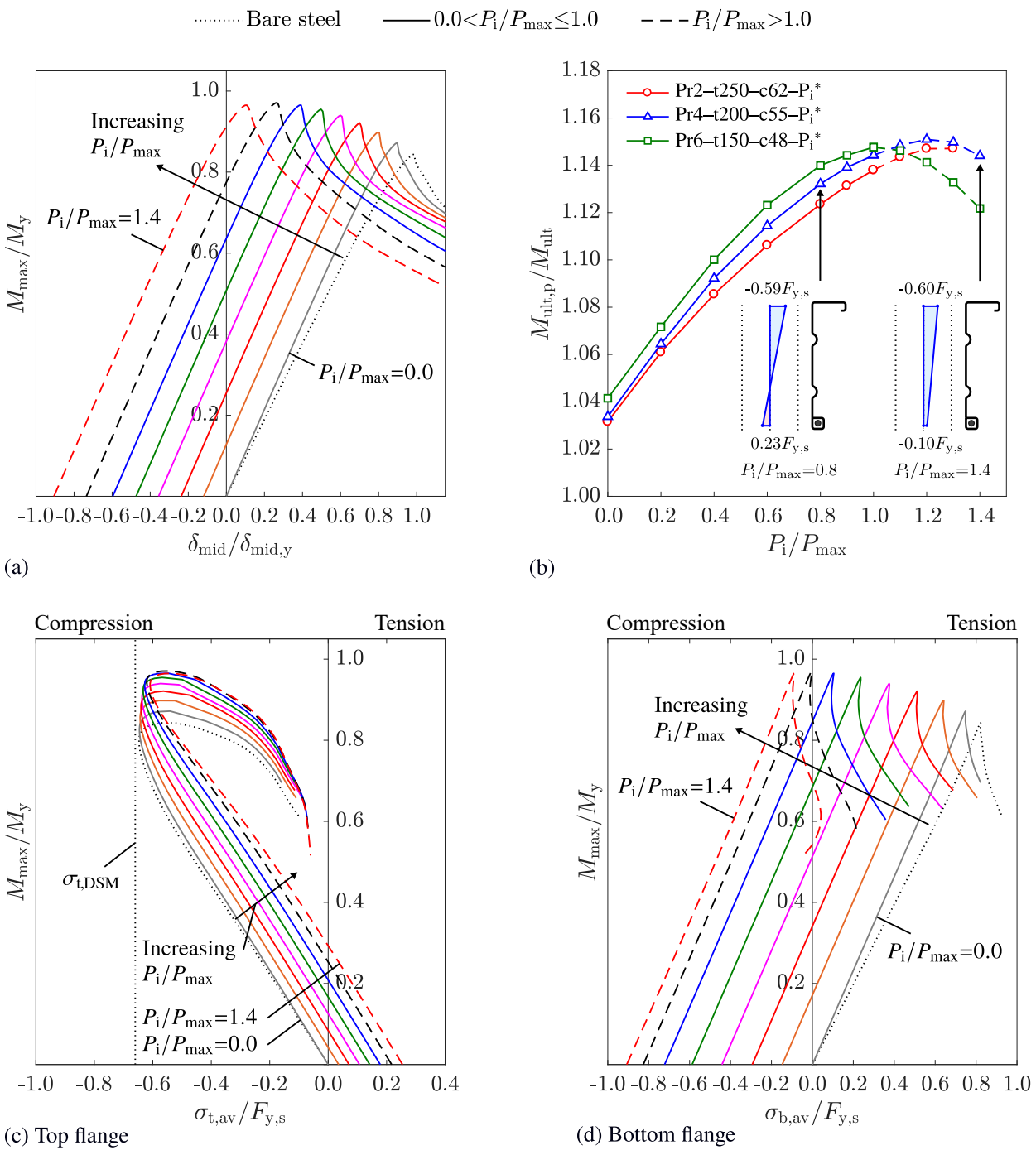


Fig. 13. FE results corresponding to the parametric study investigating the effect of the prestress level.

prestress levels. For instance, when P_i/P_{max}=1.0, the average bottom flange stress level at the ultimate point is only 10% of the yield stress.

The relationship between the moment capacity enhancement $M_{ult,p}/M_{ult}$ and the studied prestress levels is demonstrated in Fig. 13(b), where the results from two more combinations of beam geometries and cable sizes, namely Pr2–t250–c62–P_i^* and P6–t150–c48–P_i^*, are shown. In general, it may be concluded that P_{max}, as defined in Eq. 1, is a representative approximation of the prestress level that maximizes $M_{ult,p}/M_{ult}$ and thus, unless otherwise stated, it is chosen as the default prestress level in the current paper.

At very high prestress levels, a descending trend in the moment capacity enhancement can be observed in Fig. 13(b). This stems from the fact that the increasing prestress levels result in increasing negative bending, but also increasing compression of the cold-formed steel cross-section (see Fig. 3). While the net effect of prestress remains beneficial, beyond a certain level, the detrimental influence of the applied compression begins to outweigh the advantage derived from the applied negative bending. This can be seen with reference to the midspan net axial stress distributions at failure shown, for model Pr4–t200–c55 with P_i/P_{max}=0.8 and P_i/P_{max}=1.4, in idealized form in Fig. 13(b). For P_i/P_{max}=0.8, it can be seen that the top and bottom flanges are in compression and tension at failure, respectively. However, for P_i/P_{max}=1.4, the entire cross-section is under compressive stress at failure.

Effect of Cable Size

As shown in Table 5, the effect of the cable size was investigated by keeping the geometry of the cold-formed steel beam (i.e. Profile and section thickness) and the initial prestressing force constant, while varying the cable size. The latter was controlled using the normalized parameter A_c/A_s. In the present study, seven different cable sizes were considered such that:

$$A_c/A_s = \{7.0, 8.0, 10.0, 12.0, 14.0, 16.0, 18.0\} \ . \tag{5}$$

The normalized moment–deflection responses of the Pr4–t200–c*–P_i109 models, where P_i/P_{max} was kept to unity, are shown in Fig. 14(a), alongside the response of the bare steel beam. Note that only the results for A_c/A_s={7.0, 10.0, 14.0, 18.0}, which corresponds to r_c={4.5, 5.4, 6.4, 7.2} mm, and the bare steel beam are shown. It is observed that the ultimate moment capacity of the members at the end of Stage II is not influenced greatly by the cable size. However, as illustrated in the case of A_c/A_s=7.0, the use of an insufficiently large cable may result in failure of the cable in tension before the capacity of the steel beam is reached, thus compromising the capacity of the system. In the aforementioned case, failure of the cable during Stage II is caused by the incremental increase in the prestressing force ΔP, demonstrating the requirement to check the capacity of the cable during both Stages I and II. Furthermore, as expected, the presence of the cable enhances the bending stiffness of the system, as indicated by the increased gradient of the moment–deflection responses.

The normalized moment–stress responses of the Pr4–t200–c*–P_i109 models are shown in Fig. 14(b), where it is observed that as the cable size is increased, the stress level within the bottom flange decreases. This is owing to the fact that the larger the cable, the larger the proportion of the imposed vertical loading it attracts. As shown in Fig. 14(c), the utilization of the cable is dependent on its size. For instance, the use of a cable with a radius of 7.2 mm was not efficient in this case since only 45% of its tensile capacity was utilized at failure. On the other hand, as illustrated by the use of a cable with a radius of 4.5 mm, the use of an insufficiently large cable resulted in its premature failure. The optimal scenario is the one where the cold-formed steel beam and the cable

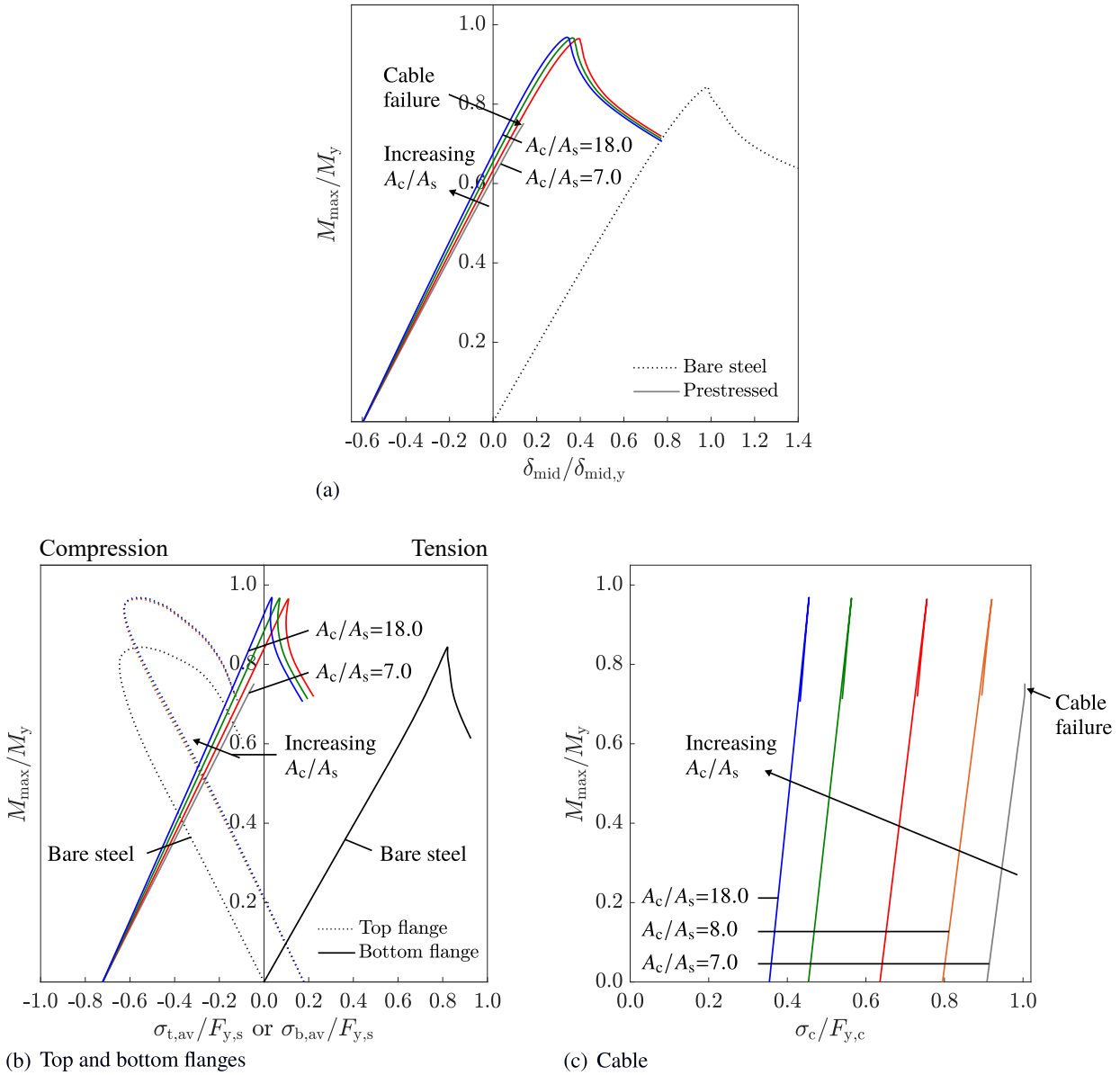


Fig. 14. FE results corresponding to the parametric study investigating the effect of the cable size.

fail simultaneously, thus fully utilizing the load-carrying capacity of both structural components of the system. In the current example, the most efficient cable size was the one with a radius of 4.8 mm, corresponding to A_c/A_s=8.0 in Fig. 14(c), since at failure σ_c=0.92$F_{y,c}$. Note that, in design calculations, suitable safety factors would of course be applied to the resistances of both the cold-formed steel beam and the cable.

Effect of Section Slenderness

As shown in Table 5, the effect of the section slenderness was investigated by varying the thickness of the cold-formed steel beam while maintaining the same cross-section profile. Hence, to keep the contribution of the cable to the bending stiffness of the system (i.e. the ratio A_c/A_s) equal to 10.5%, the size of the cable was adjusted accordingly. Furthermore, since by changing

the thickness, the maximum prestress level P_{max} that the beam can carry also changed, the initial prestressing force P_i was also adjusted to keep the ratio P_i/P_{max} equal to unity. Hence, the models utilized in the present study are defined by the notation Pr4–t*–c†–P$_i{}^\dagger$, with the thickness being varied according to Table 7, where the corresponding section slenderness values, cable radii and initial prestressing forces are listed. Note that the distortional section slenderness λ_d corresponds to positive bending. The key properties of the studied beams are listed in Appendix I, alongside the corresponding FE results.

TABLE 7. Properties of the Pr4–t*–c†–P$_i{}^\dagger$ models, where t is the controlling (variable) parameter.

t (mm)	1.00	1.25	1.50	1.75	2.00	2.25	2.50	2.75	3.00
λ_d	1.43	1.27	1.16	1.06	0.99	0.93	0.88	0.83	0.79
r_c (mm)	4.0	4.4	4.8	5.2	5.5	5.9	6.2	6.4	6.7
P_i (kN)	46	61	77	93	109	126	143	159	176

The normalized moment–deflection responses of the Pr4–t*–c†–P$_i{}^\dagger$ models, alongside the corresponding bare steel models are shown in Fig. 15(a). Note that only the results corresponding to t={1.00, 1.50, 2.00, 2.50, 3.00} mm are shown and that the value of $\delta_{mid,y}$ is the same for all models. As expected, the ultimate capacity of the bare steel beams is enhanced with increasing thickness. In the case of the prestressed beams, as the thickness is increased, the predicted capacity of the steel beam for Stage I (i.e. P_{max}) also increases, and thus a greater initial prestressing force was applied to keep P_i/P_{max} to be unity. For this reason, a larger pre-camber and a greater enhancement in the ultimate moment capacity of the steel beams are achieved with increasing thickness. Note that the moment–deflection responses of the bare steel models have the same gradient since, for each response, M_{max} is normalized by the corresponding yield moment M_y. Furthermore, the responses of the prestressed models also have the same gradient since the contribution of the cable to the system bending stiffness (i.e. the ratio A_c/A_s) was kept constant.

The parametric study presented above was repeated for the six cross-section profiles shown in Fig. 12. The variation of the moment capacity enhancement with respect to the section thickness is shown in Fig. 15(b) for the six different profiles. Overall, it is demonstrated that the thicker the cold-formed steel beam, the greater the benefit. It is also shown that the profile (i.e. the centroid location) of the steel beam also influences the benefits obtained from the addition of the prestressed cable; this effect is examined in the following sub-section.

Effect of Centroid Location

The cross-sectional geometry of prestressed steel members plays a significant role in the effectiveness of the prestressing (Hoadley 1968; Troitsky et al. 1989). If the centroid is located at the mid-height of the cross-section, the overall axial stress distribution at the end of the imposed loading stage is uneven, with the bottom flange not being fully utilized (Hadjipantelis et al. 2018a). On the other hand, as discussed below, a well-proportioned cross-section can provide increased structural benefits and thus a more economical solution. In this sub-section, to investigate the effect of the centroid location within the cross-section of the proposed beams, the six cross-section profiles shown in Fig. 12 are utilized. The origin of the benefits obtained due to the shift of the centroid location are demonstrated first and, subsequently, the parametric FE results are presented.

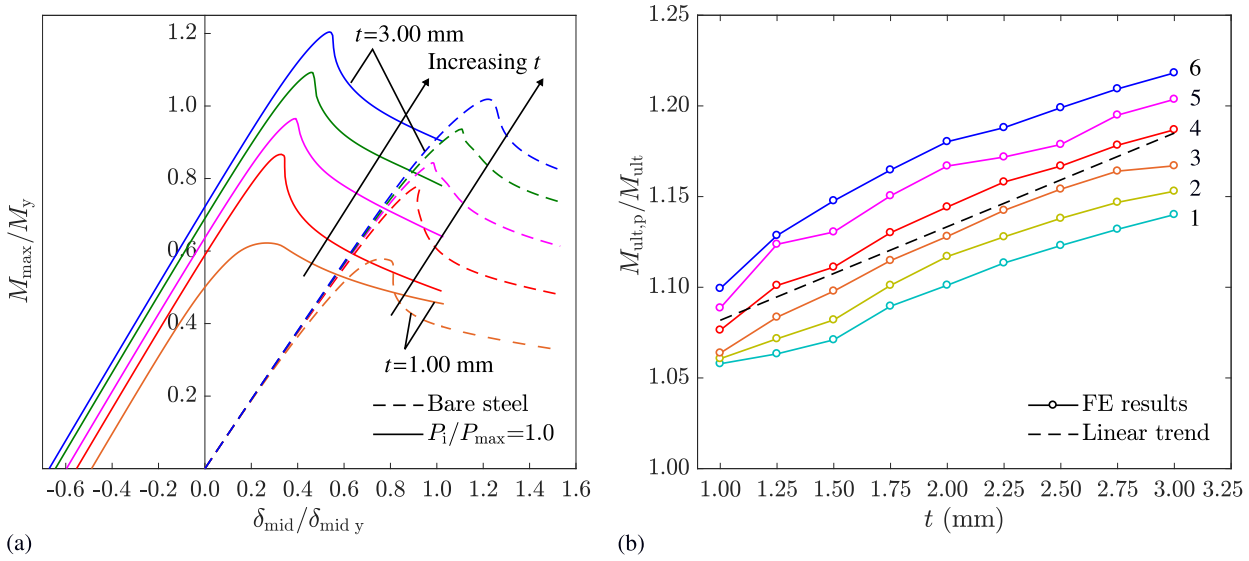


Fig. 15. FE results corresponding to the parametric study investigating the effect of the section slenderness.

Origin of obtained benefits

To illustrate the influence of the centroid location on the behavior of the proposed beams, an example is presented in Fig. 16, whereby the components of the axial stress distribution at the midspan of a prestressed beam with Profile 1 (model Pr1–t200–c55–P$_i$123) and a beam with Profile 6 (model Pr6–t200–c55–P$_i$123) are explored. The centroid of the former is located at the mid-height of the section, i.e. y_b/h=0.50, while the centroid of the latter is located at a higher location corresponding to y_b/h=0.55. The stress distributions components were determined using the linear elastic expressions shown in Fig. 3, after being normalized by the material yield stress. Note that, for illustration purposes, the components induced by ΔP are not shown herein but still have been considered in the evaluation of the overall stress levels. In both models, the same prestressing force was applied in Stage I, with the P_{max} value corresponding to Profile 1 (i.e. P_{max}=123 kN) being chosen. In Stage II, a bending moment corresponding to the yield moment of Profile 1 (i.e. M_y=32.1 kNm) was applied in both cases.

The shift of the centroid upwards has two principal effects. Firstly, the application of prestressing in Stage I becomes more effective due to the larger lever arm of the prestressing force from the strong geometric axis (compare Figs. 16(c) and (i)). Secondly, and most importantly, the application of vertical loading in Stage II imposes smaller compressive stress levels within the top flange of the beam with a higher centroid (compare Figs. 16(d) and (j)). Hence, the overall compressive stress level within the top flange at the end of Stage II is reduced (compare Figs. 16(e) and (k)). Consequently, the susceptibility of the steel beam to local/distortional buckling during loading is reduced, and thus an even greater moment is required to cause beam failure, i.e. the capacity of the beam is enhanced further.

It should be noted that the reduced compressive stress levels within the top flange during Stage II comes at the expense of increased tensile stress levels within the bottom flange. However, in the proposed prestressed beams, this increase is counteracted by the compressive stresses that are induced within the bottom flange during Stage I. As a consequence, as shown in Fig. 16(i), the

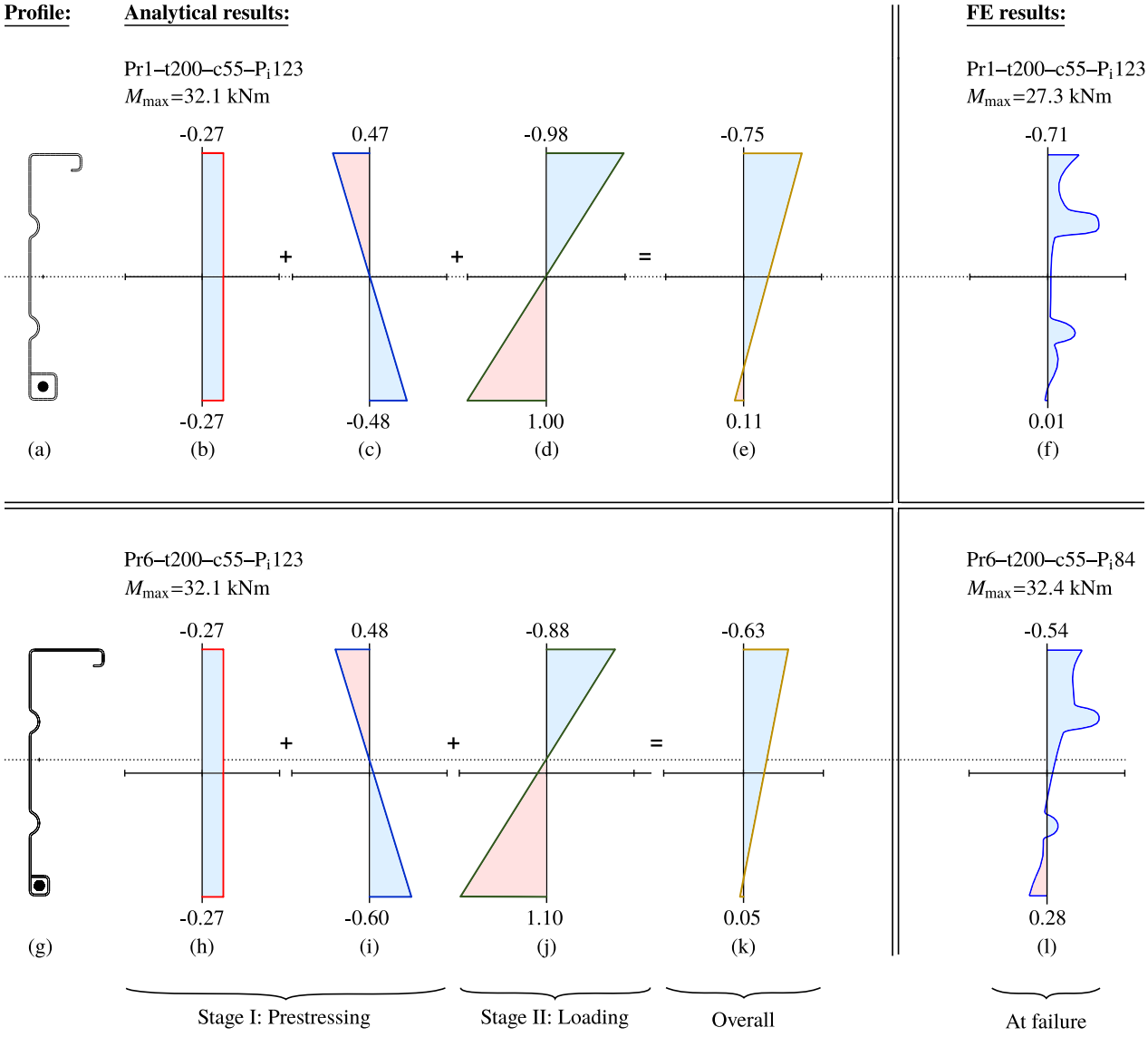


Fig. 16. Examination of the effect of the centroid location on the axial stress distribution at the critical cross-section. Axial stress distributions from the FE models at failure.

proposed system can in fact carry bending moments that are greater than the yield moment of the bare steel section.

Results from parametric study

To investigate the effect of shifting the centroid of the steel beam upwards, the cross-section profile was varied while maintaining the section thickness to be constant. Since all the profiles have the same cross-sectional area, the cable size, and thus the ratio A_c/A_s=10.5%, were also kept to be constant. Furthermore, since the maximum allowable prestressing force P_{max} for each profile is different, the initial prestressing force P_i was adjusted accordingly, with the aim of keeping the ratio P_i/P_{max} equal to unity. The key properties of the studied beams are listed in Appendix I, alongside the corresponding FE results.

The FE results from models Pr*–t200–c55–P_i† are presented below. The centroid locations y_b/h corresponding to Profiles 1–6 are given in Table 6, while the prestressing levels required to maintain the ratio P_i/P_{max}=1.0 are the following:

$$P_i = \{123, 118, 114, 109, 102, 95\} \text{ kN} . \quad (6)$$

The moment–deflection responses of the prestressed and bare steel models are shown in Fig. 17(a). Note that only the results for Profile={2,4,6}, which corresponds to y_b/h={0.51, 0.53, 0.55}, are shown. It is observed that, with increasing y_b/h, a smaller pre-camber is induced along the member during the prestressing stage. This is because, by widening the top flange of the cross-section to shift the centroid upwards, the axial compressive resistance P_n of the cold-formed steel beam is decreased, as shown in Fig. 17(b), where P_y is the squash load. Consequently, the maximum allowable prestressing force P_{max} decreases and thus, as shown in Eq. 6, a lower initial prestressing force is required to maintain P_i/P_{max} to be unity.

In Fig. 17(a), it is also observed that the higher the location of the centroid within the cross-section, the greater the moment capacity enhancement due to the addition of the prestressed cable; the origin of this increase has been discussed above. This can be examined further by studying the normalized moment–stress response of the Pr*–t200–c55–P_i† models in Fig. 17(c), where the variations of the average membrane stress levels at the top $\sigma_{t,av}$ and bottom $\sigma_{b,av}$ flanges with respect to the applied moment are shown. Firstly, it is observed that the failure of the members with higher centroids occurs at lower levels of $\sigma_{t,av}$. This is owing to the fact that these members have more slender cross-sections, thus having a lower DSM failure stress level $\sigma_{t,DSM}$. Despite that, owing to the higher centroid location, the slope of the moment–stress response of these members is greater and hence a larger moment is required to reach $\sigma_{t,DSM}$ and cause failure.

Comparing the $\sigma_{b,av}$ levels in Fig. 17(c), it is also observed that by shifting the centroid upwards, the utilization of the bottom flange is increased substantially, for instance, from approximately 5% in the case of Profile 2 to 30% in the case of Profile 6. As a result, since the bottom flange is able to carry greater proportion of the applied loading, the stress level within the cable is decreased, as shown in Fig. 17(d). Hence, an even smaller cable can be used to carry the prestressing force. This effect is also attributed to the fact that a lower prestress level is applied to the members with higher centroids.

The above observations are also illustrated in Figs. 16(f) and (l), where the axial stress distributions at the critical cross-section of the Pr1–t200–c55–P_i123 and Pr6–t200–c55–P_i84 models at failure respectively are shown. It should be noted though that the stress distributions from the FE models exhibit nonlinearity due to the occurrence of local/distortional buckling, with higher stresses observed at the locations of the intermediate stiffeners in the web. This is because, while the flat regions experience local out-of-plane deformations (i.e. buckling), the stiffeners retain their axial stiffness, thus attracting a higher proportion of the applied load. It is also worth noting that, in the case of Profile 6, a smaller part of the cross-section is subjected to compression than in the case of Profile 1 at failure. In the present example, while using the same amount of material for both the cold-formed steel beam and the cable, the ultimate capacity was increased by 18% simply by relocating some of the material of the steel beam from the bottom flange to the top flange and thus increasing y_b/h by 5%. This shift even reduces the applied prestressing force by approximately 25%, which is also beneficial.

The ultimate moment capacities achieved by the bare steel M_{ult} and prestressed $M_{ult,p}$ models with Profiles 1–6 are shown in Fig. 18(a) for three different thickness values. It is observed

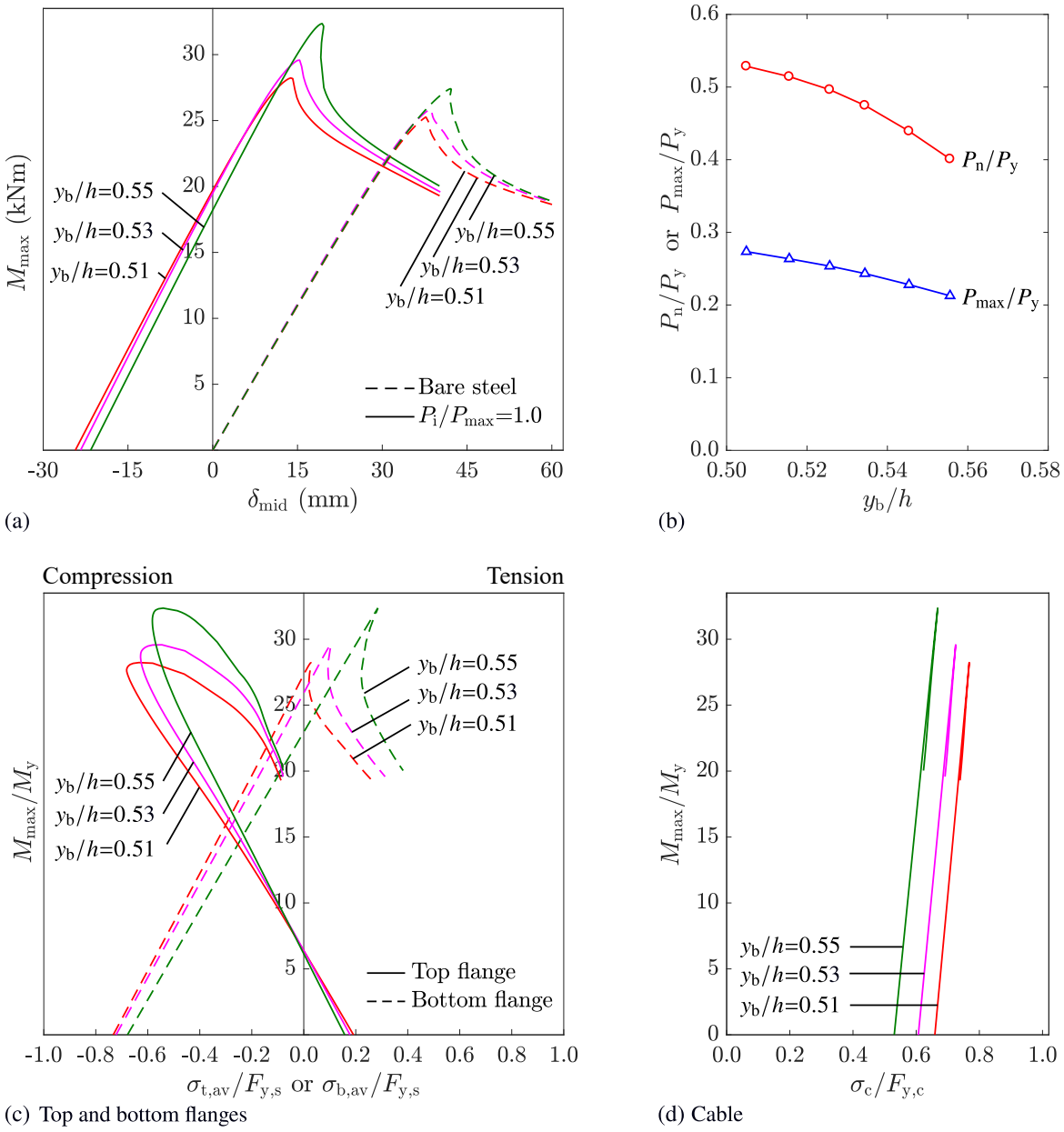


Fig. 17. FE results corresponding to the parametric study investigating the effect of the centroid location.

that, in general, as discussed earlier, the thicker the steel beam, the greater the moment capacity enhancement. The effect of the centroid location is investigated using the ratio $M_{ult,p}/M_{ult}$ (i.e. comparing the prestressed and bare steel models having the same profile) in Fig. 18(b), where it is shown that the higher the location of the centroid within the section, the greater the obtained benefits. However, since all the profiles have the same cross-sectional area, the effect of the centroid location can also be studied by comparing the capacities of the prestressed models with the capacity of the original bare steel beam (i.e. the bare steel beam with Profile 1), $M_{ult,Pr1}$, where the centroid is located at the mid-height of the section. Hence, as shown in Fig. 18(c), the ratio

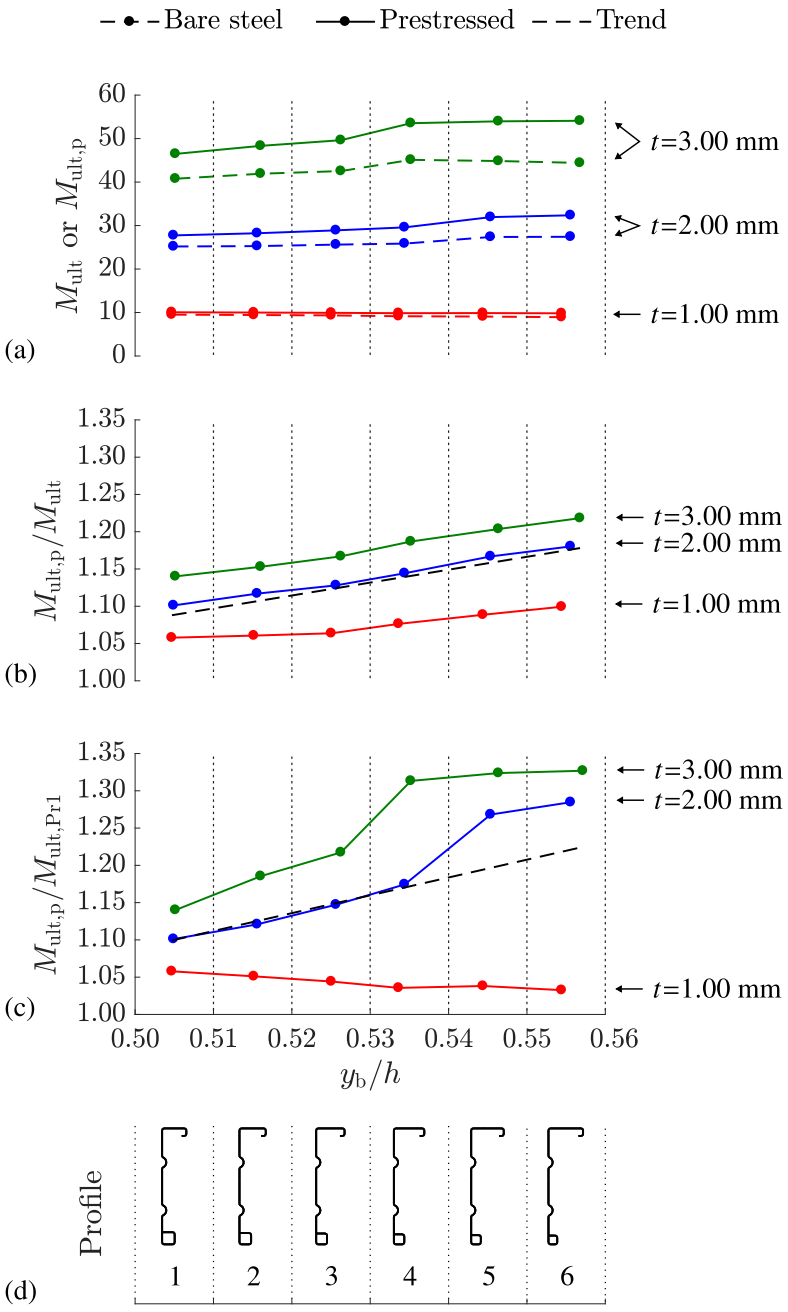


Fig. 18. Examination of the increase in the ultimate capacity of the bare steel beams with Profiles 1–6 for three different thicknesses.

$M_{ult,p}/M_{ult,Pr1}$ represents the benefits offered by the proposed concept due to both the addition of the prestressed cable and the shift of the centroid upwards, with benefits of up to approximately 35% being achieved in the case of Profile 6 and t=3.00 mm. Note that the linear trends shown as dashed lines in Figs. 18(b) and (c) were obtained by utilizing the results from the models of all nine section thicknesses.

Maximizing the Obtained Benefits

From the parametric studies presented in the previous sub-sections, it was concluded that the benefits obtained from prestressing cold-formed steel beams can be maximized by increasing: (i) the prestress level, (ii) the size of the cable, (iii) the thickness of the cold-formed steel beam, and (iv) the height at which the centroid is located within the cross-section of the steel beam. In this sub-section, the aforementioned conclusions are utilized to determine the maximum benefits that the prestressing process can offer. For this purpose, a prestressed cold-formed steel beam with the properties listed in Table 8 was modeled; this model is thus named Pr7–t400–c70–P_i^*.

TABLE 8. Properties of the Pr7–t400–c70–P_i^* model. The dimensions not listed in this table are the same with those given in Table 6.

Geometric properties:	b_1 = 22.0 mm	d_1 = 22.0 mm	b_2 = 90.0 mm
	t = 4.00 mm	e = 147.5 mm	r_c = 7.0 mm
Section properties:	y_b/h = 0.57	λ_d = 0.70	A_s = 1768 mm^2
Prestressing:	P_{max} = 205 kN	$P_n = 0.535P_y$	$M_{nx}^- = 1.0M_y$

The contribution of the cable to the system is given by the ratio A_c/A_s=8.5%, while the initial prestressing force was varied according to:

$$P_i/P_{max} = \{0.9, 1.0, 1.1, 1.2, 1.3, 1.4\}\,, \tag{7}$$

with the aim of determining the prestress level that provides the greatest increase in the capacity of the beam.

The moment–deflection responses of the Pr7–t400–c70–P_i^* models are shown in Fig. 19, alongside the responses of the corresponding bare steel model (i.e. with Profile 7) and the bare steel model with the original cross-section profile (i.e. Profile 1), whereby the centroid is located at the mid-height of the cross-section. As discussed in the previous sub-section, by comparing the prestressed models with the bare steel model with Profile 1, the benefits from both the effect of the addition of the prestressed cable and the effect of shifting the centroid upwards are considered.

As demonstrated in Fig. 19, the greatest benefit is achieved when P_i/P_{max} is equal to 1.2; hence, this is considered to be the optimized case herein. At higher prestress levels, the cable yields before the ultimate capacity of the steel beam is reached. In the optimized case, the addition of the prestressed cable increases the ultimate capacity of the original bare steel section with Profile 1 by 40% while also decreasing the deflections at the ultimate point by 53%. By comparing the prestressed beam with the corresponding bare steel section with Profile 7, the aforementioned benefits become 27% and 57% respectively. Furthermore, it is worth noting that, in the case of P_i/P_{max}=1.2, the prestressing cable and the cold-formed steel beam fail simultaneously, thus utilizing the capacities of both structural components of the system in full.

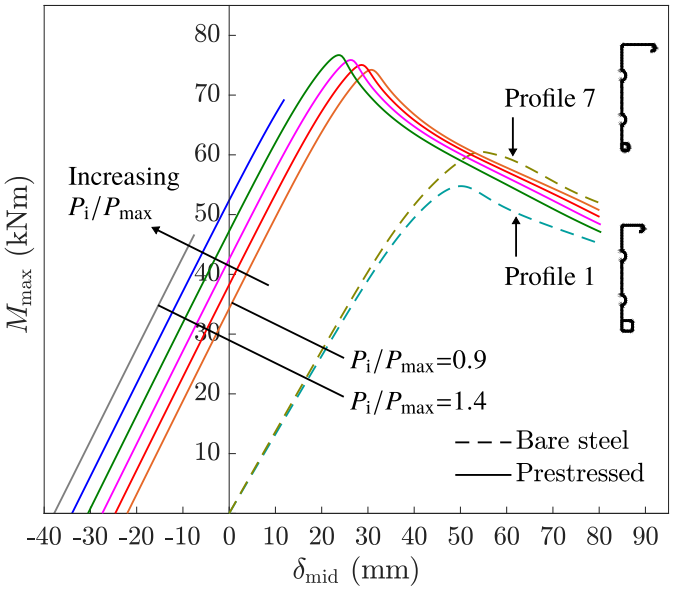


Fig. 19. Moment–deflection responses of the Pr7–t400–c70–P_i^* models with Profile 7, alongside the bare steel beam models with Profiles 1 and 7.

CONCLUSIONS

Through the application of eccentric prestressing, the performance of cold-formed steel beams can be enhanced significantly. In the proposed concept, the prestressing force is applied using a cable that is located within the bottom hollow flange of the cold-formed steel beam. The aim of the prestressing is to impose tensile stresses within the top region of the beam that counteract the compressive stresses that are induced during the subsequent vertical loading stage. Hence, the development of local instabilities is delayed and thus the member is able to carry greater loading before failure, i.e. the ultimate moment capacity of the steel beam is enhanced. The eccentric prestressing also induces a pre-camber along the beam, reducing the overall deflections of the member significantly. In addition to the material savings that the proposed beams can offer, their enhanced performance can potentially open up new opportunities for cold-formed steel in construction.

In the current paper, the principal characteristics of the proposed prestressed cold-formed beams were presented first. The development and validation of the finite element (FE) models, which have been employed to simulate the behavior of the proposed beams, were then described. Subsequently, the results from a set of parametric studies, in which the influence of the key controlling parameters has been investigated, was conducted. The effect of each parameter was analyzed in detail using the normalized moment–deflection and moment–stress responses obtained from the FE models, with the origin of the obtained benefits being demonstrated in each case.

Firstly, it was concluded that the higher the prestress level, the further the occurrence of local/distortional buckling is delayed and thus the greater the moment capacity enhancement. Secondly, it was demonstrated that an insufficiently large cable can compromise the capacity of the prestressed member and that, in the optimal scenario, the cold-formed steel beam and the cable fail simultaneously, thus utilizing the capacity of both structural components in full. Furthermore, it has been shown that a greater enhancement in the ultimate moment capacity of the steel beams can

be achieved with increasing section thickness. Finally, it was concluded that a well-proportioned cross-section can provide increased structural benefits and thus a more economical solution. In the case of the proposed beams, this can be achieved by shifting the centroid of the cold-formed steel beam upwards. The above conclusions have been utilized to demonstrate that enhancements of up to 40% in the load-carrying capacity of cold-formed steel beams and reductions of approaching 60% in their overall deflections can be achieved. In future work, the parametric FE results presented in the current paper will be used to assess the suitability of the developed design recommendations.

APPENDIX I. PARAMETRIC FE RESULTS

The key properties and FE results corresponding to the bare steel and prestressed models from the parametric studies investigating the effect of the section slenderness and centroid location are presented herein. Tables 9 and 10 correspond to Profiles 1–3 and 4–6 respectively, while $\sigma_{\mathrm{ult,p}}/F_{\mathrm{y,c}}$ is the normalized axial stress in the cable at the ultimate point.

TABLE 9. FE results for the prestressed and bare steel beams with Profiles 1–3, as shown in Fig. 12.

Profile	Geometry			Section properties			Prestressing	FE results		
	t (mm)	e (mm)	r_c (mm)	λ_d	A_s (mm^2)	M_y (kNm)	P_{max} (kN)	M_{ult} (kNm)	$M_{ult,p}$ (kNm)	$\sigma_{ult,p}/F_{y,c}$
1	1.00	126	3.95	1.42	466	16.5	51	9.5	10.2	0.63
	1.25	126	4.40	1.26	580	20.5	68	13.5	14.4	0.68
	1.50	126	4.81	1.14	693	24.4	86	17.9	19.2	0.73
	1.75	126	5.19	1.05	804	28.3	104	20.9	22.7	0.75
	2.00	126	5.53	0.97	915	32.1	123	25.2	27.7	0.79
	2.25	126	5.85	0.91	1025	35.8	142	29.7	33.1	0.82
	2.50	126	6.16	0.86	1134	39.5	161	34.3	38.5	0.84
	2.75	126	6.44	0.81	1241	43.1	179	36.5	41.3	0.85
	3.00	126	6.71	0.77	1348	46.6	198	40.8	46.5	0.87
2	1.00	130	3.94	1.41	465	16.2	49	9.4	10.0	0.61
	1.25	130	4.40	1.25	578	20.2	66	13.6	14.5	0.67
	1.50	130	4.81	1.14	691	24.0	83	17.9	19.3	0.71
	1.75	130	5.18	1.05	802	27.8	101	20.9	23.0	0.75
	2.00	130	5.52	0.97	913	31.5	118	25.3	28.2	0.77
	2.25	130	5.85	0.91	1022	35.1	136	29.8	33.6	0.79
	2.50	130	6.15	0.86	1131	38.7	154	34.6	39.4	0.82
	2.75	130	6.43	0.81	1238	42.3	172	39.6	45.4	0.84
	3.00	130	6.70	0.77	1344	45.7	191	41.9	48.3	0.85
3	1.00	133	3.94	1.43	465	16.0	48	9.3	9.9	0.61
	1.25	133	4.40	1.26	579	19.8	64	13.7	14.9	0.66
	1.50	133	4.81	1.14	691	23.6	80	18.1	19.9	0.69
	1.75	133	5.18	1.05	803	27.3	97	22.7	25.3	0.73
	2.00	133	5.52	0.98	913	31.0	114	25.6	28.9	0.75
	2.25	133	5.85	0.92	1023	34.5	131	30.3	34.6	0.77
	2.50	133	6.15	0.86	1131	38.1	149	34.9	40.3	0.80
	2.75	133	6.43	0.82	1238	41.5	166	39.9	46.5	0.82
	3.00	133	6.70	0.78	1345	44.9	183	42.5	49.6	0.83

Acknowledgments

Financial support for Nicolas Hadjipantelis was provided by the President's PhD Scholarship scheme from Imperial College London.

TABLE 10. FE results for the prestressed and bare steel beams with Profiles 4–6, as shown in Fig. 12.

Profile	Geometry			Section properties			Prestressing	FE results		
	t (mm)	e (mm)	r_c (mm)	λ_d	A_s (mm^2)	M_y (kNm)	P_{max} (kN)	M_{ult} (kNm)	$M_{ult,p}$ (kNm)	$\sigma_{ult,p}/F_{y,c}$
4	1.00	136	3.95	1.50	466	15.8	46	9.2	9.8	0.58
	1.25	136	4.40	1.27	580	19.6	61	13.8	15.2	0.63
	1.50	137	4.81	1.16	693	23.4	77	18.2	20.2	0.68
	1.75	137	5.19	1.06	804	27.0	93	22.7	25.7	0.71
	2.00	137	5.53	0.99	915	30.6	109	25.8	29.6	0.73
	2.25	137	5.85	0.93	1025	34.2	126	30.4	35.2	0.75
	2.50	137	6.16	0.88	1134	37.7	143	35.3	41.2	0.78
	2.75	137	6.44	0.83	1241	41.1	159	40.2	47.3	0.79
	3.00	137	6.71	0.79	1348	44.5	176	45.1	53.5	0.81
5	1.00	140	3.94	1.55	465	15.5	42	9.1	9.9	0.54
	1.25	141	4.40	1.29	579	19.2	57	13.8	15.5	0.61
	1.50	141	4.81	1.17	691	22.8	72	18.3	20.7	0.65
	1.75	141	5.18	1.08	803	26.4	87	22.8	26.2	0.68
	2.00	141	5.52	1.00	913	29.9	102	27.4	31.9	0.70
	2.25	141	5.85	0.94	1023	33.4	118	30.5	35.7	0.72
	2.50	141	6.15	0.89	1131	36.8	133	35.3	41.6	0.74
	2.75	141	6.43	0.84	1238	40.1	149	39.9	47.7	0.76
	3.00	141	6.70	0.80	1345	43.4	165	44.8	54.0	0.78
6	1.00	144	3.94	1.62	465	15.1	39	8.9	9.8	0.51
	1.25	144	4.40	1.30	579	18.8	53	13.6	15.3	0.57
	1.50	144	4.81	1.18	691	22.3	67	18.3	21.1	0.61
	1.75	144	5.18	1.09	803	25.8	81	22.9	26.7	0.64
	2.00	144	5.52	1.02	913	29.3	95	27.4	32.4	0.67
	2.25	144	5.85	0.95	1023	32.6	110	30.2	35.9	0.68
	2.50	144	6.15	0.90	1131	36.0	125	34.9	41.9	0.71
	2.75	144	6.43	0.85	1238	39.2	140	39.7	48.0	0.73
	3.00	144	6.70	0.81	1345	42.4	154	44.4	54.1	0.74

REFERENCES

ABAQUS (2014). "Abaqus Analysis User's Guide - Online Documentation." *Version 6.14-2, Dassault Systemes Simulia Corp.*

Afshan, S., Rossi, B., and Gardner, L. (2013). "Strength enhancements in cold-formed structural sections - Part I: Material testing." *Journal of Constructional Steel Research*, 83, 177–188.

AISI (American Iron and Steel Institute) (2016). "North American specification for the design of cold-formed steel structural members." *AISI-S100-16*.

Belletti, B. and Gasperi, A. (2010). "Behaviour of prestressed steel beams." *Journal of Structural*

Engineering, ASCE, 136(9), 1131–1139.

Camotim, D., Dinis, P. B., and Martins, A. D. (2016). "Direct strength method - a general approach to the design of cold-formed steel structures." *Recent trends in cold-formed steel construction*, C. Yu, ed., Woodhead Publishing, Chapter 4.

EN 1992-1-1 (2004). *Eurocode 2 - Design of concrete structures - Part 1-1: General rules and rules for buildings*. Brussels: European Committee for Standardization (CEN).

Gardner, L. and Ashraf, M. (2006). "Structural design for non-linear metallic materials." *Engineering Structures*, 28(6), 926–934.

Gardner, L. and Yun, X. (2018). "Description of stress–strain curves for cold-formed steels." *Construction and Building Materials*, 189, 527–538.

Gosaye, J., Gardner, L., Wadee, M. A., and Ellen, M. E. (2014). "Tensile performance of prestressed steel elements." *Engineering Structures*, 79, 234–243.

Gosaye, J., Gardner, L., Wadee, M. A., and Ellen, M. E. (2016). "Compressive behaviour and design of prestressed steel elements." *Structures*, 5, 76–87.

Hadjipantelis, N., Gardner, L., and Wadee, M. A. (2018a). "Prestressed cold-formed steel beams: Concept and mechanical behaviour." *Engineering Structures*, 172, 1057–72.

Hadjipantelis, N., Gardner, L., and Wadee, M. A. (2018b). "Prestressed cold-formed steel beams – Conceptual development." *Proceedings of the Eighth International Conference on Thin-Walled Structures*, Lisbon, Portugal, July 24-27, 2018.

Haidarali, M. R. and Nethercot, D. A. (2011). "Finite element modelling of cold-formed steel beams under local buckling or combined local/distortional buckling." *Thin-Walled Structures*, 49(12), 1554–1562.

Hancock, G. J. (2016). "Cold-formed steel structures: Research review 2013–2014." *Advances in Structural Engineering*, 19(3), 393–408.

Hill, H. N. (1944). "Determination of stress–strain relations from offset yield strength values." *National Advisory Committee for Aeronautics; Technical Note No. 927*.

Hoadley, P. G. (1968). "Development and use of prestressed steel flexural members: Part 2 - Prestressing by means of high strength steel wires or bars." *Subcommittee 3 on Prestressed Steel of Joint ASCE-AASHO Committee on Steel Flexural Members, Journal of the Structural Division, ASCE*, 94(9), 2035–2042.

Hui, C., Gardner, L., and Nethercot, D. A. (2016). "Moment redistribution in cold-formed steel continuous beams." *Thin-Walled Structures*, 98, 465–477.

Jandera, M., Gardner, L., and Machacek, J. (2008). "Residual stresses in cold-rolled stainless steel hollow sections." *Journal of Constructional Steel Research*, 64(11), 1255–1263.

Kambal, M. E. M. and Jia, Y. (2018). "Theoretical and experimental study on flexural behavior of prestressed steel plate girders." *Journal of Constructional Steel Research*, 142, 5–16.

Kyvelou, P., Gardner, L., and Nethercot, D. A. (2017). "Testing and analysis of composite cold-formed steel and wood-based flooring systems." *Journal of Structural Engineering, ASCE*, 143(11), 04017146.

Kyvelou, P., Gardner, L., and Nethercot, D. A. (2018). "Finite element modelling of composite cold-formed steel flooring systems." *Engineering Structures*, 158, 28–42.

Li, Z. and Schafer, B. W. (2010). "Buckling analysis of cold-formed steel members with general boundary conditions using CUFSM: Conventional and constrained finite strip methods." *Proceedings of the Twentieth International Specialty Conference on Cold-Formed Steel Structures*, Missouri, USA, November 3-4, 2010.

Lorenc, W. and Kubica, E. (2006). "Behavior of composite beams prestressed with external tendons: Experimental study." *Journal of Constructional Steel Research*, 62(12), 1353–1366.

Lou, T., Lopes, S. M. R., and Lopes, A. V. (2016). "Numerical modeling of externally prestressed steel–concrete composite beams." *Journal of Constructional Steel Research*, 121, 229–236.

Madrazo-Aguirre, F., Wadee, M. A., and Ruiz-Teran, A. M. (2015). "Non-linear stability of under-deck cable-stayed bridge decks." *International Journal of Non-Linear Mechanics*, 77, 28–40.

Magnel, G. (1950). "Prestressed steel structures." *The Structural Engineer*, 28, 285–295.

Mirambell, E. and Real, E. (2000). "On the calculation of deflections in structural stainless steel beams: an experimental and numerical investigation." *Journal of Constructional Steel Research*, 54(1), 109–133.

Ramberg, W. and Osgood, W. R. (1943). "Description of stress–strain curves by three parameters." *National Advisory Committee for Aeronautics; Technical Note No. 902*.

Rasmussen, K. J. R. (2003). "Full-range stress–strain curves for stainless steel alloys." *Journal of Constructional Steel Research*, 59(1), 47–61.

Riks, E. (1979). "An incremental approach to the solution of snapping and buckling problems." *International Journal of Solids and Structures*, 15(7), 529–551.

Schafer, B. W. (2008). "Review: The Direct Strength Method of cold-formed steel member design." *Journal of Constructional Steel Research*, 64(7-8), 766–778.

Schafer, B. W. (2017). "Developments in research and assessment of steel structures: Highlights from the perspective of an American researcher." *Proceedings of the Eight European Conference on Steel and Composite Structures, Eurosteel*, Copenhagen, Denmark, September 13-15, 2017.

Schafer, B. W., Li, Z., and Moen, C. D. (2010). "Computational modeling of cold-formed steel." *Thin-Walled Structures*, 48(10–11), 752–762.

Schafer, B. W. and Peköz, T. (1998). "Computational modeling of cold-formed steel: characterizing geometric imperfections and residual stresses." *Journal of Constructional Steel Research*, 47(3), 193–210.

Shifferaw, Y. and Schafer, B. W. (2012). "Inelastic bending capacity of cold-formed steel members." *Journal of Structural Engineering, ASCE*, 138(4), 468–480.

Troitsky, M. S., Zielinski, Z. A., and Rabbani, N. F. (1989). "Prestressed-steel continuous-span girders." *Journal of Structural Engineering, ASCE*, 115(6), 1357–1370.

Wadee, M. A., Gardner, L., and Osofero, A. I. (2013). "Design of prestressed stayed columns." *Journal of Constructional Steel Research*, 80, 287–298.

Wang, H. and Zhang, Y. (2009). "Experimental and numerical investigation on cold-formed steel C-section flexural members." *Journal of Constructional Steel Research*, 65(5), 1225–1235.

Wang, J., Afshan, S., and Gardner, L. (2017). "Axial behaviour of prestressed high strength steel tubular members." *Journal of Constructional Steel Research*, 133, 547–563.

Yu, C. and Schafer, B. W. (2003). "Local buckling tests on cold-formed steel beams." *Journal of Structural Engineering, ASCE*, 129(12), 1596–1606.

Yu, C. and Schafer, B. W. (2005). "Distortional buckling of cold-formed steel members in bending." *AISI-Specifications for the Design of Cold-Formed Steel Structural Members, RP05-1*, 77.

Yu, C. and Schafer, B. W. (2006). "Distortional buckling tests on cold-formed steel beams." *Journal of Structural Engineering, ASCE*, 132(4), 515–528.

Yu, C. and Schafer, B. W. (2007). "Simulation of cold-formed steel beams in local and distortional buckling with applications to the direct strength method." *Journal of Constructional Steel Research*, 63(5), 581–590.

Yu, J. and Wadee, M. A. (2017). "Mode interaction in triple-bay prestressed stayed columns." *International Journal of Non-Linear Mechanics*, 88, 47–66.